Nature Communications

https://doi.org/10.1038/s41467-026-70486-0

Article in Press

Recycling senescent cell lipids for targeted senotherapy

Received: 28 May 2025

Accepted: 27 February 2026

Cite this article as: Ji, X., He, X., Cai, H. *et al.* Recycling senescent cell lipids for targeted senotherapy. *Nat Commun* (2026). https://doi.org/10.1038/s41467-026-70486-0

Xiaoxiao Ji, Xingzi He, Honglu Cai, Peng Tang, Hao Zhou, Jiajie Wang, Yifan Wu, Jinfeng Zhou, Zhang Lin, Kaicheng Xu, Changjian Lin, Xiaoyong Wu, Kanbin Wang, Wangmi Liu, Gang Feng, Shigui Yan, Guangyao Jiang, Zihao Qu & Yiying Qi

Recycling senescent cell lipids for targeted senotherapy

Xiaoxiao Ji[1,2,3,4#], Xingzi He[1,2,3,4#], Honglu Cai[1,2,3,4#], Peng Tang[1,2,3,4], Hao Zhou[1,2,3,4], Jiajie Wang[1,2,3,4], Yifan Wu[1,2,3,4], Jinfeng Zhou[1,2,3,4], Zhang Lin[5], Kaicheng Xu[1,2,3,4], Changjian Lin[1,2,3,4], Xiaoyong Wu[1,2,3,4], Kanbin Wang[1,2,3,4], Wangmi Liu[1,2,3,4], Gang Feng[1,2,3,4], Shigui Yan[1,2,3,4], Guangyao Jiang[1,2,3,4*], Zihao Qu[1,2,3,4*], Yiying Qi[1,2,3,4,6*]

[1]Department of Orthopedic Surgery, The Second Affiliated Hospital, Zhejiang University School of Medicine, Hangzhou, Zhejiang, China.

[2]Orthopedics Research Institute of Zhejiang University, Hangzhou, Zhejiang, China.

[3]Clinical Research Center of Motor System Disease of Zhejiang Province, PR China

[4]Zhejiang Key Laboratory of Motor System Disease Precision Research and Therapy, Hangzhou City, Zhejiang Province, PR China

[5]College of chemical and biological engineering, Zhejiang University, Hangzhou 310027, China

[6]State Key Laboratory of Transvascular Implantation Devices， Hangzhou 310009, China

#These authors contributed equally: Xiaoxiao Ji, Xingzi He, Honglu Cai

*Corresponding author. Email: Yiying Qi, qiyiying@zju.edu.cn; Zihao Qu qu_z.h@zju.edu.cn; Guangyao Jiang, 11718243@zju.edu.cn

Abstract

Senescent cells (SnCs) are increasingly recognized as key contributors to osteoarthritis, with conventional strategies centered on their elimination. However, senolytic approaches face mounting limitations, driving the need for refined interventions. Here, we exploit SnCs' lipid metabolic signature to develop a senotherapeutic strategy. Given the universal lipid accumulation in SnCs and the dual role of lipids as both metabolic liabilities and essential lubricants, we engineer an injectable nanoliposuction hydrogel platform designed for "waste recycling". This system removes excess lipids to mitigate senescence-associated secretory phenotype (SASP) propagation and incorporates the harvested lipids as a pivotal component of the biomimetic lubricating system, thereby alleviating mechanical allodynia and cartilage wear. This strategy circumvents potential side effects associated with direct SnCs clearance and repurposes these traditionally harmful cells as functional resources. Our findings establish a shift in the philosophy of senescence therapy, transitioning the focus from destructive ablation to spatially adaptive reallocation of metabolites.

Introduction

Cellular senescence is a response program with broad pathophysiological relevance, triggered by various stimuli such as replicative exhaustion and diverse forms of stress[1,2,3,4,5]. Traditionally, SnCs are considered

to be in a state of irreversible growth arrest, acting as a physiological rheostat in tissue homeostasis[1,6]. Consequently, the pharmacological elimination of SnCs (senolytics) has been introduced as a key therapeutic strategy to mitigate the persistent harmful effects of pathological aging[7,8,9]. However, it is increasingly recognized that SnCs also play vital physiological roles in the body's dynamic program[10,11,12], suggesting the need for therapeutic approaches that consider their nuanced roles[10]. In addition to their secretory phenotype and epigenetic reprogramming, SnCs exhibit distinctive metabolic features, notably altered lipid metabolism, that remain underexploited for therapeutic intervention[11,13,14].

Lipid metabolic rewiring is a hallmark of SnCs[15,16] and a major driver of aging-related pathologies[17,18,19]. Yet lipids, beyond being pathological liabilities, serve essential functions in membrane composition, energy storage, signal transduction and biological lubrication[20]. Based on the almost binary "dual-sided" role of lipids in the microenvironment, we propose that leveraging the spatial and functional adaptability of lipids may offer a therapeutic strategy targeting senescence that has never been appreciated or explored. In particular, Lipid-based lubrication is a tangible therapeutic target, playing a critical role in maintaining various systems like the skin, brain, logistic channels, bones, and cartilage[21,22,23]. In this context, nanoengineered systems offer a promising platform for translating this concept, enabling the dual exploitation of lipid metabolites as both therapeutic targets and functional resources.

Capitalizing on lipid overload (cholesterol and phospholipid accumulation) in senescent chondrocytes, we developed a nanoliposuction-based senotherapeutic strategy that diverges from conventional senolytic approaches. Instead of eliminating SnCs, our methodology “slims down” senescent chondrocytes to suppress senescence propagation and repurposes recovered lipids for cartilage protection. We term this paradigm “Senorecycle,” transforming SnC-derived metabolic waste into functional resources to mitigate

disease progression (Fig.1a).

To achieve targeted lipid clearance, we identified intercellular adhesion molecule-1 (ICAM1) as a highly expressed surface marker on senescent chondrocytes. Based on this, we engineered a MINH (MβCD@ICAM1-NPs@HA/PA, named after the initials of its main components) platform. In this system, poly(lactic-co-glycolic acid) (PLGA) nanoparticles (NPs) are modified with ICAM1 monoclonal antibodies and encapsulate methyl-β-cyclodextrin (MβCD) for targeted lipid removal. The hyaluronan (HA)-based hydrogel serves as an injection and recycling system, crosslinked with poly(2-acrylamide-2-methylpropane sulfonic acid) (PAMPs) for enhanced cartilage adhesion and biomimetic lubrication (Fig.1b).

Upon injection, the hyaluronan/PAMPs hydrogel (HA/PA) anchors to cartilage surfaces and gradually releases NPs, which target senescent chondrocytes and deliver MβCD to extract accumulated cholesterol and phosphatidylcholines (PCs). This nanoparticle-driven lipid removal reduces SASP-mediated senescence transmission, as represented by Amphiregulin (Areg), and restores chondrocyte anabolic homeostasis. Extracted PCs are secreted into the joint cavity based on the natural metabolic pathway[24] and partly integrated into the hydrogel, forming a dynamic lipid reservoir. Continuous friction gradually exposes the choline head group, creating a biomimetic lubrication system with HA and lubricant (PAMPs)[25], thereby providing lipid-based hydration lubrication, reducing mechanical hyperalgesia, minimizing cartilage wear, and delaying the progression of pathological conditions (Fig.1c).

Results and Discussion

Senescent chondrocytes exhibit lipid accumulation

To characterize the universal metabolic properties of senescent chondrocytes, three in vitro and in vivo models were selected and optimized (Supplementary Fig.1a-d and Supplementary Discussion1).

Filipin staining assessed cholesterol accumulation in two chondrocyte senescence models (Supplementary Fig.1e). Also, perilipin2, a lipid-droplet associated protein, served as an indicator of lipid buildup in articular cartilage of aged mice (Supplementary Fig.1f). Then, we used BODIPY (boron-dipyrromethene) neutral lipid staining to quantify cellular cholesterol accumulation in control and senescent chondrocytes,

as well as in knee chondrocytes from young and aged mice. Higher levels of neutral lipid accumulation were observed in senescent groups (Supplementary Fig.1g-i).

Concurrently, previous studies have documented phospholipid accumulation in senescent cells and they can drive senescence progression[19]. Also, a recent study characterizing lipidomic alterations in osteoarthritic cartilage[26] revealed that phospholipids constitute 11 out of 13 upregulated lipid species, comprising 8 phosphatidylcholines (PC) and 3 phosphatidylethanolamines (PE). Building upon these findings, we quantified PC accumulation, revealing consistent upregulation of PC content across multiple chondrocyte senescence models (Supplementary Fig.1j-l).

Since peripheral cells cannot efficiently degrade cholesterol, excess cholesterol efflux is the primary means of elimination from cells[27] (Supplementary Fig.1m and Supplementary Discussion2). Therefore, we used methyl-β-cyclodextrin (MβCD) to accelerate lipid efflux. MβCD is a heptasaccharide that can extract lipids by binding to cholesterol or PC due to its hydrophobic core[28] (Supplementary Fig.1n).

However, MβCD failed to reverse the senescent phenotype, as shown by persistent SA-β-gal activity (Supplementary Fig.1o), unabated p16 protein levels (Supplementary Fig.1p), and unchanged mRNA expression of *Cdkn1a* (Supplementary Fig.1q). Nevertheless, it significantly reduced the expression of several senescence-associated secretory phenotype (SASP) genes in senescent chondrocytes (Supplementary Fig.1r), which play a critical role in osteoarthritis[2,29].

In conclusion, different senescent chondrocyte models exhibited a certain degree of lipid accumulation, represented by cholesterol and PC. While accelerating lipid efflux and extraction did not directly reverse existing cellular senescence, it reduced the expression of SASP genes in senescent chondrocytes, which holds significant potential for delaying the progression of osteoarthritis.

ICAM1 is a surface biomarker of senescent chondrocytes

Numerous studies have been conducted on chondrocyte senescence. However, none have systematically screened effective surface markers for senescent chondrocytes, leaving a significant gap in senescence-targeted treatment. Based on the three models developed in this study, we extracted membrane proteins of chondrocytes, detecting their proteomic characteristics by mass spectrometry (Fig.2a-d and Supplementary Discussion3). Next, we took the intersection of the membrane proteins upregulated in the three senescence models and arranged them by differential expression, which revealed ICAM1 as the most significantly upregulated protein across all models (Fig.2e,f). ICAM1 has been poorly studied in cartilage and was previously thought to be minimally expressed in intact articular chondrocytes[30]. Moreover, previous studies have hinted at the potential of ICAM1 as a surface marker of SnCs[31,32]. Therefore, we further characterized and quantified the membrane expression of ICAM1 in two in vitro models. Western Blotting (WB) results indicated that ICAM1 was expressed at significantly higher levels in the senescent groups of inflammation (Fig.2g) and DNA damage (Fig.2h). To determine the localization of ICAM1, we used wheat-germ agglutinin (WGA) staining on the cell membrane of chondrocytes from young and aged mice. Immunofluorescence results showed that ICAM1 was highly expressed on the surface of chondrocytes in aged mice, while its expression was nearly absent in young mice (Fig.2i). Flow cytometry further quantified a broad and significant upregulation of ICAM1 on the surface of senescent chondrocytes across three models (Fig.2j). To investigate the reliability of ICAM1 as a senescence marker of human chondrocytes, we conducted single-cell RNA sequencing analysis using two recently published datasets[33,34] (Supplementary Fig.2a-c and Supplementary Discussion4). A similar expression pattern of

ICAM1 was identified in the UMAP plot, corresponding with those chondrocytes with high senescence core scores (Fig.2k,m). Pearson correlation analysis indicated a positive correlation between *ICAM1* expression and senescence core scores in both datasets (Fig.2l: $r = 0.19$, $P<0.001$, Fig.2n: $r = 0.41$, $P < 0.001$ and Supplementary Fig.2d,e). Also, to further clarify the lipid metabolic relevance of *ICAM1*, we integrated these two scRNA-seq datasets and found that *ICAM1*-high chondrocytes exhibited significantly elevated LipidScores and enrichment in lipid metabolism–related GO and KEGG pathways (Supplementary Fig.3a-c). Consistently, senescent chondrocytes with upregulated *ICAM1* expression showed increased lipid accumulation in two senescence models (Supplementary Fig.3d,e), which establishes the foundational rationale for subsequent targeted lipid clearance strategies.

In summary, we systematically identified ICAM1 as highly expressed on the surface of chondrocytes in multiple senescent models. Through verification of multiple experiments and datasets, we clarified the potential targeting value of ICAM1 in senescent chondrocytes. At the same time, this senescence marker is expected to be further verified in other senescent cells[31], providing a reference paradigm for targeted senescence treatment.

Design and characterization of MINH

Based on the above findings, we aim to design a nanoliposuction platform targeting senescent chondrocytes for lipid waste extraction and recycling.

MβCD is widely used in biological research due to its ability to remove cholesterol[35,36,37]. However, our study repositions its underutilized physicochemical properties to pioneer therapeutic applications. First, MβCD removes both cholesterol and phospholipids[28,38,39]—the latter being critical for joint

lubrication[25,40]. Second, its structural architecture remains PC hydrophilic heads exposed during extraction, maintaining lubricative functionality[41,42]. Third, when MβCD acts directly on cells, it tends to extract lipids from plasma membranes[43], making high concentrations potentially cytotoxic. Therefore, we chose PLGA-based NPs as carriers to prevent unwanted interactions between MβCD and carriers such as biological membranes or liposomes.

MβCD@ICAM1-NPs were fabricated via double emulsion solvent evaporation, surface-conjugated with ICAM1 antibodies and encapsulating MβCD in the aqueous core (Fig.3a). The average particle size of NPs was controlled at 164.6±1.21nm to penetrate cartilage (smaller than 200 nm[44,45]) with a polydispersity index (PDI) of 0.223 (Fig.3b), and the zeta potential was -0.776±0.324mV (Fig.3c) to avoid excessively positive or negative charges interacting with cartilage matrix protein and affecting targeted delivery[45]. Antibody conjugation efficiency reached 84±3.1% (Fig.3d, Supplementary Fig.4a), while the encapsulation efficiency of MβCD in NPs was 92.13±0.067% (Fig.3e, Supplementary Fig.4b-e and Supplementary Discussion5), with sustained release of 41.13%±2% payload under physiological conditions (pH 7.4) and 53.3% ± 2.7% under OA-simulated conditions (pH 6.5 with 5 U/mL hyaluronidase) over 72 hours (Fig.3f).

To enhance the targeted delivery of NPs to cartilage, we designed an injectable HA/PA hydrogel platform (Fig.3g). HA was amine-functionalized via adipic dihydrazide (ADH) modification to obtain HA-ADH (Supplementary Fig.4f,g), which forms hydrogels with 8-arm-PEG-NHS spontaneously. PAMPs were incorporated to enhance mechanical strength, cartilage adhesion, and biomimetic lubrication (Supplementary Discussion6). Gelation kinetics assessed by vial inversion determined the appropriate ratio for hydrogel formation, which exhibited rapid gelation compatible with 25G needle injection

(Fig.3h-j and Supplementary Discussion7). Also, HA/PA hydrogel exhibited enhanced structural integrity, marked by denser crosslinking networks (Fig.3k), lower swelling capacity (Fig.3l), and superior compressive performance and recovery capability compared to HA controls (Fig.3m-p and Supplementary Discussion8). The MINH system demonstrated exceptional fatigue resistance under cyclic compression, maintaining 83.7% strain capacity retention after 300 cycles (Fig.3q), which meet the requirements of constant compression and lipid recycling. The results of SEM and confocal microscopy demonstrated the integrated structure of the MINH system and confirmed the uniform distribution of NPs in the HA/PA hydrogel (Fig.3r,s, Supplementary Fig.4h,i and Supplementary Discussion9). Finally, the release characteristics of the NPs from the MINH system revealed a two-phase profile under both physiological and OA-mimicking conditions. Approximately 55% (pH 7.4) and 63% (pH 6.5 with 5 U/mL hyaluronidase) of the payload were released within the first 3 days, followed by a sustained slow release over more than 21 days (Fig.3t), consistent with the expected degradation–release dynamics of the MINH system.

Cartilage binding affinity, biocompatibility and degradation property of MINH

Building on the interaction between HA, PAMPs (bearing negatively charged SO_3^{2-} groups), and the two major proteins (fibronectin and Col II) that constitute cartilage ECM[46], we further explored the binding ability of the MINH system to cartilage. The MINH system demonstrated sustained cartilage adhesion through HA/PA hydrogel-mediated matrix interactions, maintaining binding efficacy as hydrogel swelled (Supplementary Fig.5a). Comparative analysis of Cy5.5-labeled constructs revealed superior cartilage retention in HA/PA-based systems (HA/PA hydrogel and MINH) versus HA controls (Supplementary

Fig.5b). This enhanced interfacial affinity is expected to weaken the interfacial relationship between cartilage and hydrogels, thereby enhancing lipid transport across the interface during lipid recycling.

Biocompatibility evaluation via Live/Dead staining and CCK-8 assays confirmed MINH system maintained high cell viability with preserved proliferation capacity across all groups during 72-hour culture, showing no significant cytotoxicity (Supplementary Fig.5c-e).

The degradation rate of biomaterials determines their residence time in the body, which in turn affects their ability to perform subsequent functions. Degradation experiments in vitro indicated that HA/PA hydrogel-based systems exhibited a relatively slow degradation in the presence of hyaluronidase, with complete degradation occurring after approximately 42 days (Supplementary Fig.5f). Also, the MINH system exhibited extended in vivo retention (>30 days) surpassing HA/PA controls (Supplementary Fig.5g), which may be attributed to the role of lipids recycled by NPs.

Targeting effect of MINH on senescent chondrocytes

To evaluate the targeting effect of the MINH system on senescent chondrocytes, we conducted a series of in vitro and in vivo experiments. The senescent group exhibited a markedly higher uptake of FITC-MβCD@ICAM1-NPs than the control group (Fig.4a), and cells with elevated Cdkn2a expression within the same field of view also showed stronger fluorescence signals in two senescence models (Fig.4b). Flow cytometry was then used to provide quantitative evidence (Supplementary Fig.6a-c). Following inflammation-induced senescence, there was a significant increase in the double-positive cell population ($Cdkn2a^+$ NPs^+) (Fig.4c,d). In both the control group and the senescent group, non-senescent double-negative cells (which did not take up NPs) and senescent double-positive cells (which took up a large

number of NPs) accounted for approximately 90% of the total cells (Fig.4e). Consistent results were observed in the DNA damage-induced senescence model (Fig.4f,g,h). These findings quantitatively demonstrated that ICAM1-marked NPs could be specifically taken up by senescent chondrocytes in vitro. To further verify this targeting in ex vivo and in vivo contexts, articular cartilage explants were incubated with fluorescently labeled NPs (Fig.4i), where FITC-MβCD@ICAM1-NPs preferentially localized to chondrocytes within worn cartilage explants from osteoarthritis (OA) patients (Fig.4j). In parallel, after intra-articular implantation of MINH into the knee joints of young and aged mice (Fig.4k), aged chondrocytes exhibited significantly higher NP uptake (Fig.4l), supporting the senescence-dependent targeting behavior of the system. To visualize SnCs in vivo, p16-3MR transgenic mice were employed (Fig.4m; Supplementary Discussion10), where cartilage wear induced red fluorescence indicative of $p16^+$ chondrocytes (Fig.4n). Following MINH treatment in the ACLT model, strong co-localization between FITC-MβCD and $p16^+$ chondrocytes was observed, while GCV (ganciclovir) administration partially cleared superficial senescent cells; although the clearance effect was modest, these data collectively confirm the robust senescence-targeting capacity of MINH in vivo.

Given the complex intra-articular environment, we also examined potential nanoparticle uptake by synovial cells. Upon IL-1β stimulation mimicking OA conditions, human synovial cells and fibroblasts exhibited elevated ICAM1 membrane expression (Supplementary Fig.7a), suggesting possible NP internalization. However, chondrocytes from OA patients expressed higher ICAM1 levels than synovial cells (Supplementary Fig.7b), and considering the intrinsic cartilage affinity of MINH, these results indicated preferential chondrocyte targeting. Consistent with this, fluorescence tracking in MINH-implanted ACLT mice demonstrated predominant NP accumulation in severely worn cartilage (61.7 ±

6.06% per unit area), with markedly lower distribution in synovium (19.9 ± 3.46%) and less-damaged cartilage (18.4 ± 2.70%) (Supplementary Fig.7c,d). Although a minor fraction of NPs was internalized by synovial tissues, no cytotoxicity was observed across all tested concentrations (Supplementary Fig.7e), and NPs even reduced IL-1β–induced expression of inflammatory mediators (*MMP3*, *IL-6*, *IL-8*, *CCL2*) (Supplementary Fig.7f).

Collectively, these multi-dimensional findings demonstrate that the MINH system primarily targets senescent chondrocytes in osteoarthritis joints. Critically, even the minor fraction reaching synovial tissues exerts beneficial anti-inflammatory effects.

Nanoparticle-based lipid efflux reduces the SASP secretion landscape

Our previous study demonstrated that MβCD-mediated efflux and removal of lipids from senescent cells can reduce the expression of SASP genes in senescent chondrocytes. SASP, however, often acts as a secreted factor (not necessarily consistent with gene expression levels) that propagates senescence through paracrine signaling[29]. To further explore the direct regulatory effects of lipid efflux, chondrocytes were subjected to different stimulation conditions (Fig.5a), and the conditioned media were collected for a cytokine array screening. This array, encompassing 111 common cytokines, provided an overall view of SASP secretion profiles[47] across different treatment groups (Fig.5b). Our findings revealed that the senescent group exhibited an upregulation of most cytokines, while lipid efflux reduced upregulated SASP secretion in the senescent group (Fig.5c). Specifically, direct lipid efflux by MβCD reduced upregulated cytokines secretion by 45.6%, whereas the nanoparticle-based approach achieved an 80.7% reduction (Fig.5d and Supplementary Discussion11). This enhanced effect is likely due to the ability of nanoparticle-

based MβCD to enter cells and release slowly, offering a more controlled and comprehensive lipid clearance compared to the more "aggressive" removal of membrane lipids by free MβCD.

To explore key secretory proteins involved, we identified amphiregulin (Areg) as a key SASP effector mediating senescence propagation (Fig.5e and Supplementary Discussion12). Then, to assess the role of Areg in senescence propagation and cartilage anabolism following lipid removal by MβCD@ICAM1-NPs, we exposed normal proliferating primary chondrocytes to conditioned media from different treatments (Fig.5f). The results indicated that conditioned media from senescent chondrocytes accelerated senescence in normal proliferating chondrocytes, but this effect was diminished after lipid efflux. However, the addition of recombinant Areg protein restored the senescence-promoting effect, as confirmed by SA-β-gal staining (Fig.5g) and the expression of p16 and p21 (Fig.5h,i and Supplementary Fig.8a,b). Conversely, the expression of anabolic markers, Col2a1, Aggrecan and Sox9, followed an opposite trend (Fig.5j,k).

These findings suggested that NP-mediated lipid removal from senescent chondrocytes could reduce the secretion of SASP factors like Areg, thereby mitigating senescence propagation and promoting chondrocyte anabolism.

Direct visualization of intracellular lipid mobilization and extracellular lipid recycling

To dynamically verify the proposed lipid recycling process, we performed live-cell fluorescence imaging using fluorescently labeled MβCD and lipid analogs. Senescent chondrocytes were treated with FITC-MβCD@ICAM1-NPs and monitored for ~120 min (Supplementary Movie1). FITC fluorescence gradually accumulated over 45 minutes, partially overlapping with lysosomal markers while a

considerable fraction remained non-colocalized (Supplementary Movie1 and Supplementary Fig.9a,b), indicating that MβCD functions in both lysosomes and non-lysosomes (Supplementary Discussion13). Upon replacing the medium with NP-free solution, intracellular FITC signals progressively decreased over the next 40 minutes (Supplementary Movie1 and Supplementary Fig.9c,d), indicative of exocytosis-mediated efflux of internalized MβCD.

To track lipid mobilization, senescent chondrocytes were pre-labeled with NBD-cholesterol or NBD-phosphatidylcholine (NBD-PC), and imaging was initiated 1 h after MβCD@ICAM1-NP treatment (Supplementary Fig.10a,c). NBD-cholesterol fluorescence rapidly decreased within ~15 min (Supplementary Movie2 and Supplementary Fig.10b), whereas NBD-PC declined more gradually over ~35 min (Supplementary Movie3 and Supplementary Fig.10d), with the most pronounced membrane changes between 20–30 min (Supplementary Fig.10e), indicating active lipid externalization.

Meanwhile, Cy5.5-labeled MINH hydrogels progressively accumulated NBD-cholesterol or NBD-PC signals over time (Supplementary Movies4,5), showing delayed but continuous fluorescence enrichment that became evident after ~2 hours (Supplementary Fig.11a,b), consistent with gradual lipid release from cells and hydrogel-mediated capture.

In summary, these dynamic imaging results visualized the entire process, from MβCD@ICAM1-NPs-driven intracellular lipid mobilization and efflux to subsequent extracellular recycling by the MINH hydrogel, confirming a time-coordinated but spatially coupled process.

MINH-mediated lipid extraction and recycling for lubrication

To more accurately demonstrate the differences in the extraction and recovery of cholesterol and PC by

MINH, we employed fluorescently labeled lipids (Fig.6a and Supplementary Discussion14). The results demonstrate that the MINH system effectively releases MβCD to extract cholesterol and PC from senescent chondrocytes, with significantly higher PC or PC-MβCD complex retention in the hydrogel (Fig.6b,c and Supplementary Discussion15).

To better elucidate the spatial transport of PC between the MINH system and cartilage, the TEPC-15 antibody was used to specifically visualize choline-based phospholipids[48,49] (Fig.6d and Supplementary Discussion16). In the image, the FITC-MβCD@ICAM1-NPs released from MINH were observed to penetrate and enter into the chondrocytes of osteoarthritis explants (I). Additionally, the cross-linking between the hydrogel and the cartilage surface was clearly visible (II), weakening the distinct interface relationship. These observations align with our previous conclusions. During the "waste recycle" phase, the transport of PC (III) or the PC-MβCD complex (IV) at the cartilage interface (II) and their subsequent recovery in the hydrogel were also directly visualized (Fig.6d and Supplementary Discussion17). Furthermore, the content of PC within the hydrogel was measured to confirm the higher lipid capture efficiency of the MINH system from osteoarthritic cartilage (Fig.6e,f). Based on these findings, we visualized the three key stages of the process: the implantation of MINH and release of NPs into chondrocytes, the extraction of lipids within cells by MβCD and their recycling back into the hydrogel, and the exposure of recycled PC or its complex after hydrogel friction (Fig.6g).

Therefore, the lubricating effect of the recovered PC after friction was finally verified (Fig.6h). PC within cells was labeled with NBD-PC and co-incubated with MINH. Fluorescence microscopy revealed that NBD-PC was successfully recovered within MINH and evenly distributed (Fig.6i). When joint friction was simulated, the transfer of NBD-PC was clearly observed, with PC becoming more exposed on the gel

surface, forming a relatively continuous lipid layer (Fig.6i). This lipid transfer after friction is consistent with previous research findings[50].

Next, we conducted friction tests on the hydrogels under various conditions for 600 seconds (Fig.6h). The results revealed that hydrogels that had recovered intracellular lipids exhibited sustained low friction, with an average friction coefficient of 0.031 (Fig.6j), which is only half that of HA gels (Fig.6k). Similarly, hydrogels incubated with osteoarthritic cartilage explants also showed persistently low friction levels (Fig.6l), with an average coefficient of approximately 0.035 (Fig.6m), indicating that more lipids can be recovered from worn cartilage explants of osteoarthritis patients. These findings are indeed exciting, for this lipid repurposing strategy overcomes the limited penetration of externally applied liposomes[44,50] (Supplementary Discussion18,19), leveraging natural metabolite secretion pathways and weakened material-biointerfaces to transform accumulated lipids into functional lubricants.

Effect of MINH treatment on osteoarthritis

Then, a series of experiments were designed to test whether MINH implantation could delay the progression of ACLT-induced traumatic osteoarthritis (Fig.7a). First, we conducted a series of behavioral experiments. The results of the open field test and the hot plate test did not reach statistical significance (Supplementary Fig.12a-f and Supplementary Discussion20). The von Frey testing was used to determine the mechanical pain sensation through the paw withdrawal threshold (Supplementary Fig.12g). The results suggested that MINH significantly improved the mechanical hyperalgesia compared to other groups (Supplementary Fig.12h,i). In addition, gait pattern analysis of different treatment groups found that hydrogel implantation did not affect the normal walking of mice (Supplementary Fig.12j), and the

right paws of mice in the MINH treatment group showed a larger contact area, suggesting relief from pain-related muscle weakness (Supplementary Fig.12k). In conclusion, MINH treatment can alleviate some pain-related behaviors associated with osteoarthritis, particularly improving mechanical hyperalgesia.

Next, micro-computed tomography (micro-CT) was used to examine the knee joint in transverse, coronal, and sagittal planes (Fig.7b). The medial compartment of the tibial subchondral bone was selected for subsequent analysis, and the results showed that MINH treatment slowed morphological changes of the subchondral bone plate in the ACLT model and reduced osteophyte formation (Fig.7b). Meanwhile, quantitative analysis showed that the MINH treatment inhibited subchondral bone remodeling (Fig.7c) and prevented increases in total tissue volume (TV) and trabecular pattern factor (Tb.pf) due to traumatic arthritis (Fig.7d,e). It also mitigated the loss of subchondral bone plate thickness (Fig.7f). The in vivo effects were more pronounced than those observed in mice treated with NPs or HA/PA hydrogel alone. Safranin-O staining provided a more intuitive view of the cartilage destruction in the same area of different treatment groups (Fig.7g), and the Osteoarthritis Research Society International (OARSI) score quantitatively demonstrated the cartilage protection effect of MINH treatment (Fig.7h). At last, we performed immunohistochemical analysis on joint sections (Fig.7i), revealing that MINH treatment alleviated the loss of Col2a1 and Aggrecan in the articular cartilage area (Fig.7j,k). This indicated that MINH effectively inhibited the decline in chondrocyte anabolic capacity in ACLT mice, consistent with in vitro results.

Subsequently, we evaluated the MINH system's efficacy in modulating lipid content under arthritic conditions (Supplementary Fig.13a). Following therapeutic intervention, flow cytometric analysis of

harvested murine cartilage revealed a significant reduction in neutral lipid deposition such as cholesterol (Supplementary Fig.13b,c), and MINH also reduced the content of PC in arthritis cartilage (Supplementary Fig.13d and Supplementary Discussion21). Concluding the study, we documented the surgical implantation protocol (Supplementary Fig.14a) and confirmed systemic biocompatibility through comprehensive organ safety assessments (Supplementary Fig.14b). We further evaluated the systemic biosafety of the treatment through hematological and biochemical analyses. All measured parameters, including indicators of immune response (white blood cell and lymphocyte counts), renal function (blood urea nitrogen), and liver/tissue damage (alanine aminotransferase, lactate dehydrogenase, creatine phosphokinase), remained within normal ranges (Supplementary Fig.14c,d). These results confirm the treatment's favorable biocompatibility.

In summary, the above in vivo experiments show that MINH implantation therapy has promising prospects and effects. It reduces mechanical hyperalgesia associated with traumatic osteoarthritis and provides long-term cartilage protection, alleviating wear on articular cartilage and loss of chondrocyte function.

Senorecycle therapy overcomes the limitations of Senolytics

In the final section, we comprehensively compared the advantages of the nanoliposuction-based senorecycle therapy over traditional senotherapy in osteoarthritis (Fig.8a). In the context of chondrocyte senescence, although senolytics represent a promising therapeutic approach[9], it exhibits notable limitations and translational challenges[51]. Previous investigations have predominantly focused on the regenerative microenvironment established by senescent cell elimination[9]. However, the consequences of

cleared cells should be critically re-examined[52], as the dense extracellular matrix of articular cartilage fundamentally restricts immune-mediated clearance pathways.

Initial in vitro senescent cell clearance using Dasatinib and Quercetin (D+Q)[7,8,53] revealed that both MβCD@ICAM1-NPs and classical senolytics (Supplementary Fig.15a,b and Supplementary Discussion22) effectively suppressed the expression of SASP-related genes (*IL-6*, *Mmp13* and *Ccl2*) across two senescence models (Supplementary Fig.16a,b), while enhancing the gene expression of *Col2a1* and *Aggrecan* (Supplementary Fig.16c,d), suggesting microenvironmental remodeling post-clearance. Paradoxically, cytokine profiling of conditioned media demonstrated increased secretion levels of most inflammatory proteins (IL-6, Mmp9 and Mmp13) and the major DAMP protein Hmgb1 following clearance interventions (Fig.8b,c and Supplementary Fig.16e), implying potential impacts of cleared senescent cells.

Subsequently, to assess the long-term effects of senescent-cell clearance independent of lingering senescence-inducing stimuli, we examined normally proliferating primary chondrocytes (~10% senescent cells) (Fig.8d). In this setting, senolytic treatment triggered rapid accumulation of proinflammatory factors (IL-6, Mmp9, Mmp13) and DAMPs (Hmgb1) within 24 hours, demonstrating progressive accumulation over 4 days, while MβCD@ICAM1-NPs conversely preserved physiological secretion patterns (Fig.8e). Corresponding analysis of chondrogenic gene expression under sustained culture conditions (without medium replacement) revealed early matrix deterioration in senolytic-treated groups, characterized by persistently elevated expression of *IL-6* and *Mmp13*, alongside suppressed *Aggrecan* and *Col2a1* expression as early as Day 2 (Fig.8d,f). These data suggest conventional senolytic treatment drives chronic microenvironmental inflammation through sustained proinflammatory and DAMP accumulation,

impairing functional homeostasis of neighboring chondrocytes over extended durations (Supplementary Discussion23), potentially explaining their limited clinical efficacy. Comparatively, targeted nanoliposuction therapy demonstrated sustained efficacy.

Tribological assessment of joint cavity microenvironments using cartilage explants (Fig.8g) revealed MINH's superior lubrication performance versus senolytic treatment (Supplementary Movie6), maintaining ultralow friction coefficients for sustained chondroprotection (Fig.8h). Lastly, therapeutic outcomes between senolytic treatment and MINH therapy were compared in p16-3MR transgenic mice (Fig.8i). GCV treatment failed to alleviate mechanical allodynia – likely attributable to persistent post-clearance elevation of proinflammatory factors and DAMPs (Fig.8j). Micro-CT analysis revealed that GCV treatment partially ameliorated subchondral bone sclerosis without modifying subchondral bone thickness, while MINH implantation exhibited superior therapeutic efficacy (Fig.8k, Supplementary Fig.16f,g). Safranin-O staining and OARSI scoring further confirmed MINH's enhanced articular cartilage preservation (Fig.8l, Supplementary Fig.16h). Immunohistochemistry demonstrated that MINH treatment markedly upregulated anabolic markers (Aggrecan, Col2a1) while suppressing catabolic (Mmp13) and inflammatory (IL-6) protein expression compared to conventional therapy (Fig.8m, Supplementary Fig.16i).

In conclusion, our findings systematically delineate the inherent limitations of traditional senotherapies and establish the comprehensive therapeutic superiority of nanoliposuction-based senotherapy for osteoarthritis intervention.

Collectively, this study introduces a senescence-targeted treatment that capitalizes on the metabolic

characteristics of SnCs, specifically their lipid accumulation. By identifying ICAM1 as a reliable surface marker for senescent chondrocytes and developing the MINH system, we offer a targeted approach that removes lipid accumulation while simultaneously leveraging these lipids for lubrication within the joint. This "Senorecycle" strategy represents a significant shift in senescence-targeted therapies, moving beyond mere cell elimination to harnessing SnCs for functional contributions to tissue repair. With the capacity for wide-scale application, this therapy holds immense clinical promise not only for osteoarthritis but also for broader senescence-related pathologies. This development introduces a versatile nanotechnology framework for precision medicine, offering a translatable therapeutic concept with far-reaching implications for future clinical interventions.

Methods

Ethics statement

All experiments involving human subjects and animals were approved by the Ethics Review Committee and the Animal Ethics Committee of the Second Affiliated Hospital of Zhejiang University School of Medicine, respectively. The study was conducted in accordance with all relevant ethical regulations.

Chondrocyte culture and senescence model

Primary chondrocytes were isolated from the femoral condyles and tibial plateaus of 6-day-old mice. Digestion and culture procedures were strictly followed according to standardized protocols[54], and P1 chondrocytes were used for in vitro experiments to prevent phenotypic differences caused by the dedifferentiation of primary chondrocytes. Primary chondrocytes were generally maintained at a density

of 20 × 10^3 cells/cm^2 in a sterile incubator at 37°C with 5% CO_2 to prevent contact inhibition due to excessive density.

Recombinant IL-1β (ABclonal, RP01340) was used to induce inflammatory senescence in primary chondrocytes[55]. To reduce the apoptotic effect induced by IL-1β, the stimulation conditions were optimized. The best inflammatory senescence phenotype of chondrocytes was observed with an IL-1β concentration of 10ng/ml for 24 hours.

Bleomycin (Cayman Chemical, 13877) was used to induce DNA damage-related senescence in primary chondrocytes at a concentration of 10μg/ml for 24 hours[37]. Consistent with previous literature, chondrocytes exhibited obvious senescence phenotypes under these conditions.

Knee cartilage from young mice (4-6 weeks) or aged mice (18-20 months) was directly used to characterize cartilage senescence in vivo. The age of young and aged mice within the same experiment was kept consistent. Articular cartilage was sliced, or chondrocytes were isolated and extracted according to the needs of subsequent experiments.

Expression levels of senescence-related and SASP-related genes

Total RNA was isolated from cells using an RNA extraction kit (Qiagen), and RNA was reverse transcribed into cDNA using the One Step RT-PCR Kit (ACCURATE BIOTECHNOLOGY (HUMAN), AG11606) as previously described[56]. Quantitative PCR was performed according to the manufacturer's instructions. Actb was used as an endogenous normalization control. The primer sequences used are listed in Supplementary Table 2 (included in the supplementary information file).

Extraction of membrane proteins and LC-MS/MS analysis

The low abundance and hydrophobicity of membrane proteins pose challenges in handling, which can be a bottleneck for LC-MS/MS identification. We extracted and purified cell membranes following the latest protocols[57]. Subsequently, proteomic analysis of membrane proteins was performed on control and senescence groups across the three models. LC-MS/MS analysis was conducted using a Q Exactive mass spectrometer (Thermo Scientific) coupled with an Easy nLC system (Proxeon Biosystems). The mass spectrometer operated in positive ion mode. MS data were acquired using a data-dependent top 20 method, dynamically selecting the most abundant precursor ions from the survey scan (300-1800 m/z) for HCD fragmentation. The instrument was operated with peptide recognition mode enabled. The MS raw data for each sample were combined and analyzed using MaxQuant 1.6.14 software for identification and quantitation. The SwissProt mouse protein sequence database, containing 17,144 entries (downloaded on January 3, 2023), was used for the initial search. For secondary confirmation of membrane proteins, confidence scores higher than 3 (range 0-5) were determined using the UniProtKB mouse "membrane" protein sequence database (Supplementary Data 1), containing 7,414 entries (downloaded on December 10, 2023), as described in previous literature[58]. The results are provided in Supplementary Data 2-4 for subsequent analysis and screening. The specific upregulated proteins identified in the pairwise intersections of the differentially expressed proteomes from the three senescence models are comprehensively listed in Supplementary Table 1 (included in the supplementary information file).

Proteomics data analysis

All downstream proteomics data analyses were conducted using R language (version 4.3). Unsupervised

clustering was performed using PCA (Principal Component Analysis) to verify the reliability of the grouping and the consistency within the groups. Protein expression levels with an absolute Log_2 fold-change ≥ 0.5 (corresponding to ≥1.41-fold change) and an adjusted P-value < 0.05 were considered differentially expressed proteins (DEPs), including both upregulated and downregulated proteins. The visualization of differentially expressed proteins was presented using heatmaps and volcano plots, created with the ComplexHeatmap[59] and ggplot2 packages. In the present study, no missing value imputation was performed prior to differential expression analysis. Gene Ontology (GO) enrichment analysis for upregulated and downregulated proteins was performed using the ClusterProfiler package (v4.10.1)[60]. GO enrichment analysis included biological process (BP). A P-value < 0.05 and a false discovery rate (FDR) < 0.1 were considered statistically significant.

Antibody and drugs

Nanoparticle modification

ICAM-1 monoclonal antibody (R&D Systems, BBA3 or Abcam, ab171123) was modified onto the surface of nanoparticles to achieve different targeting requirements.

Western blot

ICAM1 (ABclonal, A20472, 1: 1000), Na/K-ATPase β1 (Cell Signalling Technology, #44759, 1:1000), Cdkn2a (Proteintech, 10883-1AP, 1:1000), Cdkn1a (Santa Cruz, Sc-6246, 1:150), beta-actin (Boster Biological Technology, BM0627), Aggrecan (ABclonal, A8536, 1:500), Col2a1 (Proteintech, 28459-1-AP, 1:1000), Sox9 (ABclonal, A19710, 1:1000)

Immunofluorescence

ICAM1 (ABclonal, A23661, 1: 100), Cdkn2a (Santa Cruz, Sc-1661, 1:180), TEPC-15 primary antibody (Sigma, M1421)

Flow cytometry

ICAM1 (ABclonal, A25857, 1: 200), Cdkn2a (Abcam, ab108349, 1:200)

Drugs

MβCD (MCE, HY-101461, 50μg/mL), Dasatinib (MCE, HY-10181, 200nM), Quercetin (MCE, HY-18085, 10μM)

Immunofluorescence of mouse joint tissue

Knee joint samples from young and aged mice were collected. After fixation and decalcification, the samples were embedded in paraffin and cut into 5μm thick sections. Antigen retrieval was performed using 0.1% trypsin without EDTA at 37°C for 1.5 hours. Following blocking with 10% BSA at room temperature for 1 hour, the sections were incubated with primary antibody (ABclonal, A23661, 1: 100) overnight at 4°C. The next day, Alexa 488-conjugated goat anti-mouse secondary antibody (Invitrogen, A11001, 1:500) was used for incubation at room temperature for 1 hour. iFluor 594-Wheat Germ Agglutinin (WGA) (AAT Bioquest, 25550) and DAPI (Invitrogen, F6057) were then used to stain the cell membrane and nucleus, respectively. Fluorescence confocal microscopy was used to image and analyze.

Human scRNA-seq data preprocessing and analysis

Gene expression matrices [GSE220243, GSE255460] were processed using Seurat (v5.0.2)[61]. Ribosomal genes were removed. Cells were filtered with cutoffs of a minimum of 300 genes per cell and a maximum

of 20% mitochondrial reads. Genes per cell, transcript counts per cell, and mitochondrial read percentages per cell are presented in Supplementary Fig.2. Seurat was used for dimensionality reduction and cell clustering. Harmony[62] was applied to correct for batch effects, and 25 principal components were used for RunUMAP and FindNeighbors. The AddModuleScore function of the Seurat package was used to calculate the senescence core score for each chondrocyte. The senescence core gene set included CDKN1A and CDKN2A. Chondrocyte cells that expressed ICAM1 were filtered for gene expression correlation analysis. Pearson correlation analysis was used for calculating gene expression correlation.

Mouse XL cytokine array for secreted proteins

Primary chondrocytes were divided into four groups: the normal proliferation group, the senescence group (treated with IL-1β), the senescence + MβCD (50 μg/mL) group, and the senescence + MβCD@ICAM1-NPs group (with MβCD content matching the previous group). Conditioned medium was collected from each group after centrifugation at 700 × g for 10 minutes at 4°C. To measure the SASP, the conditioned medium was analyzed using the Mouse XL Cytokine Array Kit (R&D, ARY028). The relative levels of 111 cytokines and chemokines were measured and quantified. The array procedure and data analysis were conducted according to the manufacturer's instructions.

Amphiregulin-mediated propagation of senescence

Four types of conditioned media were prepared: the supernatant from the normal proliferation group, the senescence group, the senescence + lipid clearance (MβCD@ICAM1-NPs) group, and the senescence + lipid clearance group + Areg recombinant protein (R&D system, 989-AR-100, 200 ng/mL). These

conditioned media were co-cultured with primary P0 chondrocytes. Cellular senescence was assessed by SA-β-gal staining and the expression of senescence-related proteins (Cdkn2a and Cdkn1a) as previously described. The anabolism of chondrocytes was evaluated by Western blotting for Aggrecan, Col2a1, and Sox9 proteins.

Phosphatidylcholine assay

The PC content was examined using the PC Assay Kit (Abcam, ab83377). According to the instructions of the reagent manufacturer, the PC content in cells or cartilage tissues under different treatments was detected. To determine the recovered PC content in the hydrogels, three groups were set up: the HA/PA hydrogels incubated with cartilage explants from OA patients, the MINH system incubated with cartilage explants from OA patients, and the MINH system incubated with explants from non-arthritic patients. All samples were incubated for 24 hours under the previously described conditions. The hydrogels from each group were collected, fully lysed, and resuspended in the assay buffer. The samples were then centrifuged at 14,000 × g for 5 minutes at 4°C, and the supernatant was mixed with assay buffer, PC hydrolase, PC development mixture, and OxiRed probe. The PC content of each sample was determined and calculated according to the manufacturer's instructions.

Tribology testing

Different hydrogel samples were affixed to the bottom of a 6-cm diameter culture dish using cyanoacrylate glue, and tribological tests were conducted using a universal material testing machine (UMT-3, Bruker, Germany) in a reciprocating sliding manner. A CoCr alloy ball with a diameter of 6 mm was employed as

the mating surface to ensure consistency across all tests. To simulate the physiological pressure of the joint (up to 25 MPa), an average load of 1 N was applied. The hydrogel sample was secured in place, and the CoCr alloy ball reciprocated for 600 seconds at a frequency of 1 Hz over a stroke length of 5 mm. Each test group was repeated three times in parallel. When observing lipid transfer, chondrocytes were labeled with NBD-PC as previously described, incubated with the MINH system, and the MINH was then removed and fixed in the culture dish. The distribution of NBD-PC in the hydrogel was observed using a fluorescence microscope before friction. After friction, the changes in the distribution of NBD-PC were observed again under the same conditions. The conditions for testing the friction coefficient of cartilage explants with different treatments were the same as above.

ELISA assay

Following experimental interventions, conditioned media were harvested from each treatment group. Secretory profiles of IL-6 (ABclonal, RK04845), Mmp9 (ABclonal, RK00187), Mmp13 (ABclonal, RK09313), Ccl2 (ABclonal, RK00381), Hmgb1 (Thermo Scientific, EEL102) were quantitatively assessed per manufacturer's specifications. After appropriate dilution with assay buffer, optical density measurements were acquired using a Tecan Spark multimode microplate reader, with data processing performed through SparkControl Magellan V3.1 software.

In vivo animal experiments

C57BL/6J mice were selected for the relevant in vivo experiments, with mice of the same sex and age randomly assigned to each experimental group. All interventions were conducted by researchers who were

blinded to the group assignments. Animal studies were performed in accordance with ethical regulations and protocols approved by the Animal Ethics Committee of the Second Affiliated Hospital of Zhejiang University School of Medicine. Mice were housed in cages with no more than five mice per cage, individually ventilated, and maintained on a 12-hour light-dark cycle. The room temperature and relative humidity were kept constant, and the animals had free access to food and water.

Anterior cruciate ligament transection (ACLT) surgery was used to induce osteoarthritis models in mice. General anesthesia was administered with 3% isoflurane, and aseptic surgery was performed after shaving the hind limbs. For the sham group, the patellar tendon was exposed by making an incision in the medial joint capsule, the knee joint was exposed, and the incision was closed with sutures. For ACLT surgery, after opening the joint capsule, the anterior cruciate ligament was transected using microscissors under a surgical microscope, and the skin incision was sutured. The drawer test was performed to confirm the success of the model.

In this study, 8-week-old male mice were used, with eight mice in each experimental group. Sham surgery or ACLT surgery was performed according to the experimental design. The mice were randomly divided into five groups: sham surgery group, HA/PA hydrogel injection group after surgery (HA/PA), nanoparticle injection group after surgery (MβCD@ICAM1-NPs), vehicle group after surgery (PBS), and complete system MINH injection group after surgery (MβCD@ICAM1-NPs@HA/PA). Based on the retention time in the body, treatment was administered twice: once at 1 week and again at 4 weeks after surgery. The mice were euthanized at 8 weeks post-surgery, and the joints were collected for evaluation.

Microcomputed tomography (Micro-CT) and analysis

Knee joint samples were collected and fixed in 4% PFA for 48 hours. Micro-CT (Bruker SKYSCAN1276) was used to scan the knee joint specimens from each group of mice. The X-ray energy was set to 180μA/60 kV, and the isometric resolution was set to 10 μm according to the instrument manual. CTAn and CTVol software were used to perform 3D modeling, with the medial compartment of the tibial subchondral bone selected for analysis. The same position was chosen to display the coronal, transverse, and sagittal planes. The structural parameters analyzed included total tissue volume (TV), trabecular pattern factor (Tb.pf), and subchondral bone plate thickness (SBP.Th).

Histological staining and immunohistochemistry

Knee joint samples from each group were fixed, decalcified, and dehydrated. The samples were then embedded in paraffin, and 5 μm thick sagittal sections of the medial joint were prepared. The medial tibial plateau was stained with Safranin O-Fast Green, and histological scoring was conducted by three blinded observers according to the OARSI grading system (0-6). Immunohistochemistry was used to evaluate the levels of Aggrecan and Col2a1. The stained sections were imaged using a microscope, and the positive areas in representative images were quantified using Image J. Additionally, the heart, liver, spleen, lungs, and kidneys of the experimental animals were collected for H&E staining to evaluate biosafety.

Statistical analysis

The letter "n" indicates the number of biologically independent samples. The sample size for each experiment, specific statistical tests, and main effects of statistical analysis are detailed in the figure legends. Data are presented as mean ± sd. Statistical comparisons between two independent groups were

performed using the unpaired or paired two-tailed Student's t-tests. Multiple comparisons were conducted using one-way analysis of variance (ANOVA) with post hoc Tukey or Dunnett's tests. Data based on the ordinal grading system were analyzed using the two-tailed nonparametric Mann–Whitney U test. Statistical analyses were performed using GraphPad Prism v.10.0, and exact P values are provided in the figures. Statistical significance was set at $P < 0.05$. For Fig.3k,r; 4a,b and 6c,d,i, each experiment was independently repeated at least three times with similar results.

Data availability

The main data supporting the findings of this study are presented in the paper and its supplementary information. The raw mass spectrometry proteomics data generated in this study have been deposited in the iProX database (https://www.iprox.cn/), under accession number IPX0012242000. Source data are provided with this paper.

References

1. Di Micco, R., Krizhanovsky, V., Baker,D. & d'Adda di Fagagna, F. Cellular senescence in ageing: from mechanisms to therapeutic opportunities. *Nat. Rev. Mol. Cell Biol.* **22**, 75–95 (2021).
2. Coryell, P.R., Diekman, B.O. & Loeser, R.F. Mechanisms and therapeutic implications of cellular senescence in osteoarthritis. *Nat. Rev. Rheumatol.* **17**, 47–57 (2021).
3. Mehdizadeh, M., Aguilar, M., Thorin, E., Ferbeyre, G. & Nattel, S. The role of cellular senescence in cardiac disease: basic biology and clinical relevance. *Nat. Rev. Cardiol.* **19**, 250–264 (2022).

4. Schmitt, C. A., Wang, B. & Demaria, M. Senescence and cancer - role and therapeutic opportunities. *Nat. Rev. Clin. Oncol*. **19**, 619–636 (2022).

5. Sanfeliu-Redondo, D., Gibert-Ramos, A. & Gracia-Sancho, J. Cell senescence in liver diseases: pathological mechanism and theranostic opportunity. *Nat. Rev. Gastroenterol. Hepatol*. **21**, 477–492 (2024).

6. López-Otín, C., Blasco, M. A., Partridge, L., Serrano, M. & Kroemer, G. Hallmarks of aging: An expanding universe. *Cell* **186**, 243–278 (2023).

7. Chaib, S., Tchkonia, T. & Kirkland, J.L. Cellular senescence and senolytics: the path to the clinic. *Nat. Med.* **28**, 1556–1568 (2022).

8. Colville, A. et al. Death-seq identifies regulators of cell death and senolytic therapies. *Cell Metab*. **35**, 1814–1829 (2023).

9. Jeon, O. et al. Local clearance of senescent cells attenuates the development of post-traumatic osteoarthritis and creates a pro-regenerative environment. *Nat. Med.* **23**, 775–781 (2017).

10. de Magalhães, J. P. Cellular senescence in normal physiology. *Science* **384**, 1300–1301 (2024).

11. Reyes, N. S. et al. Sentinel *p16*$^{INK4a+}$ cells in the basement membrane form a reparative niche in the lung. *Science* **378**, 192–201(2022).

12. Wang, X. et al. Signalling by senescent melanocytes hyperactivates hair growth. *Nature* **618**, 808–817 (2023).

13. Rabinovitch M. Are Senolytic Agents Guilty of Overkill or Inappropriate Age Discrimination? *Circulation* **147**, 667–668 (2023).

14. Reimann, M., Lee, S. & Schmitt, C. A. Cellular senescence: Neither irreversible nor reversible. *J. Exp.*

Med. **221**, e20232136 (2024).

15. Hornburg, D. et al. Dynamic lipidome alterations associated with human health, disease and ageing. *Nat. Metab.* **5**, 1578–1594 (2023).
16. Tsugawa, H. et al. A lipidome landscape of aging in mice. *Nat. Aging* **4**, 709–726 (2024).
17. Byrns, C.N. et al. Senescent glia link mitochondrial dysfunction and lipid accumulation. *Nature* **630**, 475–483 (2024).
18. Kaffe, E. et al. Bioactive signalling lipids as drivers of chronic liver diseases. *J. Hepatol*. **80**, 140–154 (2024).
19. Zeng, Q. et al. Lipids and lipid metabolism in cellular senescence: Emerging targets for age-related diseases. *Ageing Res. Rev*. **97**, 102294 (2024).
20. Jeon, Y. G., Kim, Y. Y., Lee, G. & Kim, J. B. Physiological and pathological roles of lipogenesis. *Nat. Metab.* **5**, 735–759 (2023).
21. Yang, L., Zhao, X., Ma, Z., Ma, S. & Zhou, F. An overview of functional biolubricants. *Friction* **11**, 23–47 (2023).
22. Gebeshuber, I.C. & Van Aken, G. Editorial: Friction and Lubricants Related to Human Bodies. *Lubricants* **2017**, *5*, 4 (2017).
23. DeMoya, C.D. et al. Advances in viscosupplementation and tribosupplementation for early-stage osteoarthritis therapy. *Nat. Rev. Rheumatol.* **20**, 432–451 (2024).
24. Robinson, W. et al. Low-grade inflammation as a key mediator of the pathogenesis of osteoarthritis. *Nat. Rev. Rheumatol.* **12**, 580–592 (2016).

25. Seror, J. et al. Supramolecular synergy in the boundary lubrication of synovial joints. *Nat. Commun.* **6**, 6497 (2015).

26. Zhou, Q. et al. Lipidomics unravels lipid changes in osteoarthritis articular cartilage. *Ann. Rheum. Dis*. S0003-4967(25)00054-8. Advance online publication (2025).

27. Wei, G. et al. Risk of metabolic abnormalities in osteoarthritis: a new perspective to understand its pathological mechanisms. *Bone Res.* **11**, 63 (2023).

28. Monnaert, V., Tilloy, S., Bricout, H., Fenart, L., Cecchelli, R. & Monflier, E. Behavior of alpha-, beta-, and gamma-cyclodextrins and their derivatives on an in vitro model of blood-brain barrier. *J. Pharmacol. Exp. Ther*. **310**, 745–751 (2004).

29. Wang, B. et al. The senescence-associated secretory phenotype and its physiological and pathological implications. *Nat. Rev. Mol. Cell Biol.* (2024).

30. Davies, M. E., Sharma, H. & Pigott, R. ICAM-1 expression on chondrocytes in rheumatoid arthritis: induction by synovial cytokines. *Mediators Inflamm*. **1**, 71–74 (1992).

31. Suryadevara, V. et al. SenNet recommendations for detecting senescent cells in different tissues. *Nat. Rev. Mol. Cell Biol.* (2024).

32. Gorgoulis, V. et al. p53-Dependent ICAM-1 overexpression in senescent human cells identified in atherosclerotic lesions. *Lab. Invest.* **85**, 502–511 (2005).

33. Swahn, H. et al. Senescent cell population with ZEB1 transcription factor as its main regulator promotes osteoarthritis in cartilage and meniscus. *Ann. Rheum. Dis*. **82**, 403–415 (2023).

34. Fan, Y. et al. Unveiling inflammatory and prehypertrophic cell populations as key contributors to knee cartilage degeneration in osteoarthritis using multi-omics data integration. *Ann. Rheum. Dis*. **83**, 926-944 (2024).

35. Zhang, Bc. et al. Cholesterol-binding motifs in STING that control endoplasmic reticulum retention mediate anti-tumoral activity of cholesterol-lowering compounds. *Nat.Commun.* **15**, 2760 (2024).

36. Hu, X. et al. Bitter taste TAS2R14 activation by intracellular tastants and cholesterol. *Nature* **631**, 459–466 (2024).

37. Roh, K. et al. Lysosomal control of senescence and inflammation through cholesterol partitioning. *Nat. Metab.* **5**, 398–413 (2023).

38. Doktorova, M. et al. Preparation of asymmetric phospholipid vesicles for use as cell membrane models. *Nat. Protoc.* **13**, 2086–2101 (2018).

39. Bozelli, J. C., Jr, Hou, Y. H. & Epand, R. M. Thermodynamics of Methyl-β-cyclodextrin-Induced Lipid Vesicle Solubilization: Effect of Lipid Headgroup and Backbone. *Langmuir* **33**, 13882–13891 (2017).

40. Lin, W. & Klein, J. Recent Progress in Cartilage Lubrication. *Adv. Mater*. **33**, e2005513 (2021).

41. Sett, R., Paul, B. K. & Guchhait, N. Unsaturation of the phospholipid side-chain influences its interaction with cyclodextrins: A spectroscopic exploration using a phenazinium dye. *Colloids Surf. B. Biointerfaces* **180**, 150–158 (2019).

42. Szente, L. & Fenyvesi, É. Cyclodextrin-Lipid Complexes: Cavity Size Matters. *Struct. Chem.* **28**, 479–492 (2017).

43. Abe, M. & Kobayashi, T. Imaging cholesterol depletion at the plasma membrane by methyl-β-cyclodextrin. *J. Lipid Res*. **62**, 100077 (2021).

44. Lei, Y. et al. Injectable hydrogel microspheres with self-renewable hydration layers alleviate osteoarthritis. *Sci. Adv*. **8**, eabl6449 (2022).

45. Bajpayee, A. & Grodzinsky, A. Cartilage-targeting drug delivery: can electrostatic interactions help?. *Nat. Rev. Rheumatol.* **13**, 183–193 (2017).

46. Xie, R. et al. Biomimetic cartilage-lubricating polymers regenerate cartilage in rats with early osteoarthritis. *Nat. Biomed. Eng.* **5**, 1189–1201 (2021).

47. Moiseeva, V. et al. Senescence atlas reveals an aged-like inflamed niche that blunts muscle regeneration. *Nature* **613**, 169–178 (2023).

48. Shaw, P. X. et al. Complement factor H genotypes impact risk of age-related macular degeneration by interaction with oxidized phospholipids. *Proc. Natl Acad. Sci. USA* **109**, 13757–13762 (2012).

49. R, Liuzzi. S, Gallier. S, Ringler. S, Caserta. & S, Guido. Visualization of choline-based phospholipids at the interface of oil/water emulsions with TEPC-15 antibody. *RSC Adv.* **6**, 109960 —109968 (2016).

50. Lin, W. et al. Cartilage-inspired, lipid-based boundary-lubricated hydrogels. *Science* **370**, 335–338 (2020).

51. Dolgin, E. Send in the senolytics. *Nat. Biotechnol.* **38**, 1371–1377 (2020).

52. McHugh, D., Gil, J. Senescence and aging: Causes, consequences, and therapeutic avenues. *J. Cell. Biol*. **217**(1), 65–77 (2018).

53. Zhao, J. et al. Senolytics cocktail dasatinib and quercetin alleviate chondrocyte senescence and facet joint osteoarthritis in mice. *Spine J*. **25**(1), 184–198. (2025).

54. Gosset, M. et al. Primary culture and phenotyping of murine chondrocytes. *Nat. Protoc.* **3**, 1253–1260 (2008).

55. Arra, M. et al. IκB-ζ signaling promotes chondrocyte inflammatory phenotype, senescence, and erosive joint pathology. *Bone Res.* **10**, 12 (2022).

56. Ji, X. et al. GSTP1-mediated S-glutathionylation of Pik3r1 is a redox hub that inhibits osteoclastogenesis through regulating autophagic flux. *Redox Biol.* **61**, 102635 (2023).

57. Kongpracha, P. et al. Simple But Efficacious Enrichment of Integral Membrane Proteins and Their Interactions for In-Depth Membrane Proteomics. *Mol. Cell Proteomics* **21**, 100206 (2022).

58. Amor, C. et al. Senolytic CAR T cells reverse senescence-associated pathologies. *Nature* **583**, 127–132 (2020).

59. Gu, Z., Eils, R. & Schlesner, M. Complex heatmaps reveal patterns and correlations in multidimensional genomic data. *Bioinforma. Oxf. Engl.* **32**, 2847–2849 (2016).

60. Wu, T. et al. clusterProfiler 4.0: A universal enrichment tool for interpreting omics data. *Innov. Camb. Mass* **2**, 100141 (2021).

61. Hao, Y. et al. Dictionary learning for integrative, multimodal and scalable single-cell analysis. *Nat. Biotechnol.* **42**, 293–304 (2024).

62. Korsunsky, I. et al. Fast, sensitive and accurate integration of single-cell data with Harmony. *Nat. Methods* **16**, 1289–1296 (2019).

Acknowledgments

This work was supported by grants from the National Nature Science Fund of China (82201729 to Z.Q., 82501891 to J.H., 8251101103 to Safwat Adel Abdo Moqbel, 82072413 and 82101649 to Y.Q.), the Natural Science Foundation of Zhejiang Province (LMS25H060001 to Y.Q.), the Key R&D Program of Zhejiang Province (2021C03108 to G.F.), and the Joint Construction Project of Zhejiang Province and Health Ministry (WKJ-ZJ-2029 to G.F.). We thank Safwat Adel Abdo Moqbel for providing financial support during the revision of this article. We thank Professor Ruikang Tang from Zhejiang University for his invaluable help in clarifying and structuring the research ideas for this paper. We thank Ms. Xiaoye Li and the Center for Basic and Translational Research at the Second Affiliated Hospital of Zhejiang University School of Medicine for their laboratory management and technical support. We thank Ms Xiaoxing Wu from the Small Animal Experiment Center of the Second Affiliated Hospital of Zhejiang University School of Medicine for her valuable assistance with our animal studies. We thank Turtle Tech Ltd. (Shanghai, China) for their technical guidance on PCR and for their assistance with primer design and validation. We thank Shanghai Applied Protein Technology Co., Ltd. for their help with proteomics, Jingyao Chen from the core facility plat form of Zhejiang University School of Medicine for their technical support and Shanghai Bioprofile Technology Co., Ltd. for their help with scRNA-seq analysis.

Author contributions

X.J., X.H., P.T., Y.W., J.Z., K.X., C.L., X.W. and K.W. performed the experimental operations. X.J. and H.C. performed the analysis and visualization of the single-cell data. X.J., Z.Q., J.W. and Z.L. completed the design and preparation of MINH. X.J. and H.Z. completed the related experiments and analysis of p16-3MR mice. Y.Q., Z.Q., G.J., S.Y., W.L. and G.F. supervised this project. X.J. conceived and designed

the study. X.J. and Y.Q. completed the conceptual integration and manuscript writing.

Competing interests

The authors declare no competing interests.

Figure Legends

Fig.1 Schematic diagram of Targeted Senorecycle Therapy.

a, The mechanistic distinction between traditional senolytics therapy and targeted senorecycle therapy: Rather than directly inducing senescent cell apoptosis, the senorecycle strategy implements cellular "lipid offloading" to reduce pathological lipid accumulation in senescent cells, while repurposing extracted PC as resources for cartilage protection. b, Key components of the MINH system and their respective functional roles. c, The detailed mechanism of MINH-mediated targeted lipid extraction ("liposuction") and subsequent lipid repurposing for joint lubrication.

Fig.2 ICAM1 is a surface biomarker of senescent chondrocytes

a, Workflow of membrane protein extraction and proteomic analysis. b, Principal component analysis (PCA) of proteomes of three cartilage-related senescence models. c, Volcano plot of differentially expressed proteins across models. Each point represents a protein; significantly upregulated proteins are highlighted. d, GO term (Biological Process) enrichment analysis of upregulated and downregulated proteins. e,f Venn diagram of upregulated proteins across models (e) and fold change of representative proteins from pairwise intersections (f). ICAM1 was identified. g, Western blotting and quantification of

ICAM1 in membrane proteins of inflammation-related (IL-1β treatment) chondrocyte senescence. n=6 biologically independent cell cultures (mean ± s.d.). h, Western blotting and quantification of ICAM1 in membrane proteins of DNA damage-related (bleomycin treatment) chondrocyte senescence. n=5 biologically independent cell cultures (mean ± s.d.). i. Left: Fluorescence images of ICAM1 in the articular cartilage of young and aged mice (nuclei, DAPI; membrane, WGA). The white dotted line insets in the images are shown enlarged in the right panels. Right: The fluorescence of ICAM1 and WGA staining (cell membrane) is distributed along the yellow line, indicating the localization of ICAM1 on the membrane (top). Quantitative comparison of ICAM1-positive cells in cartilage regions of young and aged mice (bottom). n=3 mice per group; each data point represents an individual mouse (mean ± s.d.). j, Flow cytometry (left) and quantification (right) of ICAM1 surface expression in three models. n=6–9 biologically independent cell cultures as indicated (mean ± s.d.). k,l,m,n Correlation analysis of *ICAM1* with senescence core score using scRNA-seq dataset from GSE220243 (k,l) and GSE255460 (m,n). k,m, Patterns of senescence core markers and *ICAM1* of chondrocyte cells with UMAP plot. l,n, Pearson's correlation analysis shows *ICAM1* is positvely correlated with the senescence core score. Each spot represents an individual chondrocyte. The *P* values and correlation coefficients were calculated using two-tailed Pearson's correlation analysis. The GO enrichment *P* values were calculated using Fisher's exact test and adjusted for multiple comparisons using the Benjamini–Hochberg procedure. Other *P* values were determined using a two-tailed unpaired Student's t-test (c,g-j). Source data are provided as a Source Data file.

Fig.3 Design and characterization of MINH

a, Schematic diagram of the synthesis of MβCD@ICAM1-NPs. b, Size distribution (Left) and TEM images (Right) of MβCD@ICAM1-NPs (scale bar, top: 50μm, bottom: 50nm) (n=3, mean ± s.d.). c, Zeta potential distribution of MβCD@ICAM1-NPs (n=3, mean ± s.d.). d, Conjugation efficiency of ICAM1 monoclonal antibody. n=3 independent experiments (mean ± s.d.). e, Encapsulation efficiency of MβCD in NPs. n=3 independent experiments (mean ± s.d.). f, Release curves of MβCD releasing from NPs under pH 7.4 and pH 6.5 + 5 U/mL hyaluronidase conditions (n=3, mean ± s.d.). g, Schematic diagram of the hydrogel (HA/PA) synthesis process. h, Images of the formation of HA hydrogel and HA/PA hydrogel (Left, HA-ADH:8-arm-PEG-NHS=9:1; Right: HA-ADH:8-arm-PEG-NHS:PAMPs=9:1:1). i, Gelation time of hydrogels with different polymer ratios at 37 ℃. j, Image of the injectability of HA/PA hydrogel. k, SEM images of hydrogels with different polymer ratios (scale bar, 50μm). l, Swelling rates of hydrogels with different polymer ratios (n=3, mean ± s.d.). m, Uniaxial stress–strain curves of hydrogels compressed until rupture. n, Compression modulus of different hydrogels. n = 3 independent experiments (mean ± s.d.). o, Uniaxial compression-relaxation curves of different hydrogels (The area enclosed by the curve represents the energy dissipation.). p, The HA/PA hydrogel was subjected to 20 consecutive cycles of compression–relaxation without any waiting time between each cycle. q, Cyclic compression curves of HA/PA hydrogel with 30% strain for 300 cycles. r, SEM image of the MINH system, including HA/PA hydrogel and MβCD@ICAM1-NPs (scale bar, 1μm. Yellow pseudo-color represents NPs in the hydrogel). s, 3D fluorescence image of uniform distribution of FITC-MβCD@ICAM1-NPs in Cy5.5-HA/PA hydrogel (scale bar, 100μm). t, Release profiles of NPs from HA/PA hydrogels under pH 7.4 and pH 6.5 + 5 U/mL hyaluronidase conditions over 35 days in vitro. Source data are provided as a Source Data file. *P* value was determined from one-way ANOVA with a Tukey post-hoc test (n).

Fig.4 Targeting effect of MINH on senescent chondrocytes

a, Representative fluorescence images of nanoparticle (FITC-MβCD@ICAM1-NPs) uptake in control and senescence group (Bleomycin). Cdkn2a as senescence marker (scale bar, 50μm). b, In the same field of view, nanoparticle uptake by cells with different Cdkn2a levels in two senescence models; higher senescence leads to more uptake (scale bar, 20 μm). c,d, Flow cytometry (c) and quantification (d) of NP uptake in inflammation-related senescence model. n=5 biologically independent cell cultures (mean ± s.d.). e,h, Flow cytometric analysis of senescence-targeting in inflammation-related (e) and DNA damage-related (h) models, highlighting double-negative and double-positive populations. f,g, Flow cytometry (f) and quantification (g) of NP uptake in DNA damage-related senescence model. n=5 biologically independent cell cultures (mean ± s.d.). i, Scheme of human cartilage explant preparation and treatment workflow. j, MINH (FITC-MβCD@ICAM1-NPs@HA/PA) system incubated with normal and arthritic cartilage explants, with FITC-MβCD@IgG-NPs@HA/PA as control. Representative images and quantification show differential nanoparticle penetration. n=3 biologically independent cartilage explants per group (mean ± s.d.). k, MINH system was injected into the knee joints of young and aged mice, respectively. The knee joints were collected for sample preparation and observation. l, Representative fluorescent images and quantification (n=3, mean ± s.d.) of nanoparticle penetration in the knee cartilage of young and aged mice (white dashed area highlights superficial cartilage difference; inverted color for clarity.). m, Workflow of MINH targeting in ACLT model using p16-3MR mice. n, Representative images and quantification of NP targeting in various groups, including wild-type mouse with sham operation, wild-type mouse with ACLT + MINH, p16-3MR mouse with ACLT + MINH, p16-3MR mouse with sham

operation + MINH, and GCV (ganciclovir) depletion group (Red: p16 positive; Green: FITC-MβCD@ICAM1-NPs). Bottom right: Analysis of multiple areas of co-localization of p16 and nanoparticle fluorescence in the p16-3MR mouse with ACLT operation + MINH treatment group. *P* values were determined from planned pairwise comparisons using a two-tailed unpaired Student's t-test (d,g,l,n) or one-way ANOVA with a Tukey post-hoc test (j). Source data are provided as a Source Data file.

Fig.5 Nanoparticle-based lipid efflux reduces the SASP secretion landscape

a, Schematic diagram of the cell processing and supernatant collection process. b,c, The cytokine array was used to detect the differences in cell secretion proteins in different groups, including the supernatants of the control group, senescence group, senescence + MβCD group, and senescence + MβCD@ICAM1-NPs group (b), The heat map was used to visualize the expression differences of SASP in the whole cell supernatant across different groups (c). d, The pie chart shows the reduction in SASP secretion after depletion of senescent cell lipids using MβCD and MβCD@ICAM1-NPs, with the former reducing it by 45.6% (Left) and the latter by 80.7% (Right). e, The key SASP with the most significant differences after lipid removal was identified. According to the fold difference, SASPs upregulated after senescence stimulation (Left), SASPs downregulated after MβCD treatment (Middle), and SASPs downregulated after MβCD@ICAM1-NPs treatment (Right) is arranged respectively. The red dashed box highlights the top potential key SASP-Amphiregulin. f, Schematic diagram of the process of collecting conditioned medium from different treatments and co-culturing with untreated primary chondrocytes. g, Following the treatments above, SA-β-gal staining (Left) and quantification (Right) results of primary chondrocytes

in conditioned medium. n=4 independent experiments (mean ± s.d.). h,i Western blot and quantification results of aging-related p16 and p21. n=3 independent experiments (mean ± s.d.). j,k Western blot and quantification results of cartilage anabolism-related Aggrecan, Col2a1 and Sox9. n=3 independent experiments (mean ± s.d.). *P* values were determined from planned pairwise comparisons using a two-tailed unpaired Student's t-test (g,i,k). Source data are provided as a Source Data file.

Fig.6 MINH-mediated lipid extraction and recycling for lubrication

a, Schematic diagram of the recovery process of labeled lipids in chondrocytes using the MINH system. b, In inflammation-related (Left) and DNA damage-related (Right) chondrocyte senescence, pie charts of the distribution ratios of cholesterol (top) and phosphatidylcholine (bottom) in cells, cell supernatants, and MINH. c, Representative fluorescence images of phosphatidylcholine and cholesterol recovered by the MINH system (PC, NBD; cholesterol, Cy3.5; MINH, Cy5.5). d, Representative multicolor fluorescence images of MINH system incubated with OA patient cartilage explants (nuclei, DAPI; MβCD, FITC; Hydrogel, Cy5.5; PC, TEPC-15), and the white dotted line insets in the images are shown enlarged in the right panels. I: White arrows indicate FITC-MβCD@NPs delivered into chondrocytes. II: The white dashed box represents the interface where the hydrogel is cross-linked with the cartilage explant, where phosphatidylcholine and FITC-MβCD can be observed during transport. III: White arrows indicate PC storage depots that are recycled into the hydrogel. IV: White arrows indicate the PC-MβCD complex recycled into the hydrogel. e, Schematic diagram of the process of recovering PC from human cartilage explants with different systems. f, Quantitative results of PC recovered in different systems. n=5 independently prepared samples (mean ± s.d.). g, Schematic diagram of the three processes of the MINH

platform acting on cartilage explants. h, Schematic diagram of friction coefficient detection of MINH system with recovered PC. i, NBD-PC labeled chondrocytes, induced senescence and incubated with the MINH system. Representative fluorescence images of hydrogels with NBD-PC before (top) and after (bottom) friction. j,k, COF-time curves of pure HA hydrogel, pure HA/PA hydrogel, pure MINH system, and MINH system incubated with aged chondrocytes (j), along with quantitative results of the average COF (k) of each system. n=3 independent experiments (mean ± s.d.). l,m, COF-time curves of normal cartilage explants and worn cartilage explants (from osteoarthritis patients) after incubation of MINH system (l), as well as quantitative results (m) of average COF. n=3 independent experiments (mean ± s.d.). *P* values were determined using a two-tailed unpaired Student's t-test (m) or one-way ANOVA with a Tukey post-hoc test (f,k). Source data are provided as a Source Data file.

Fig.7 Effect of MINH treatment on osteoarthritis

a, Schematic diagram of the experimental design for establishing a surgical model of osteoarthritis in mice and evaluating the cartilage-protective effect of MINH. b, Representative micro-CT images of the knee joints of mice in each group, including the coronal (first row), transverse (second row), and sagittal (third row) planes of the tibial subchondral bone, and the knee joints after 3D reconstruction (fourth row). The markedly hyperplastic osteophytes are pseudo-colored in red. c, Visualization results of the medial subchondral bone plate of the knee joint of each group of mice. The red pseudo-color shows its thickness, and the heat map shows the distribution of its bone density (top). The morphology and density of the trabeculae of the medial subchondral bone plate visualized from the transverse planes (bottom). All comparisons are based on the same location of the sample. d,e,f, Quantitative results of the total tissue

volume (TV) (d), trabecular pattern factor (Tb. Pf) (e) and subchondral bone plate thickness (SBP. Th) (f) of the medial subchondral bone in each group of mice at 8 weeks after surgery (n=8, mean ± s.d.). g, Representative images of Safranin-O staining results of knee joint sections of mice in each group 8 weeks after surgery. The same position (black dotted box) in the above image is enlarged and shown below. h, Quantitative results of the medial tibial plateau joint score based on OARSI (n=8, mean ± 95%CI). i, Representative images of immunohistochemical staining (Aggrecan and Col2a1) of medial tibia sections from knee joints of mice in each group 8 weeks after surgery. j,k, Quantitative analysis of tissue immunochemistry results of Aggrecan (j) and Col2a1(k) positive areas (n=6, mean ± s.d.). *P* values were determined using two tailed nonparametric Mann–Whitney U test (h) or one-way ANOVA with a Tukey post-hoc test (d-f,j,k). Source data are provided as a Source Data file.

Fig.8 Senorecycle therapy overcomes the limitations of Senolytics

a, Schematic comparing targeted senorecycle therapy vs. senolytics: targeting, non-apoptotic lipid extraction, sustained efficacy, dual chondroprotection-lubrication. b, Experimental workflow for comparative analysis: Following mild senescence (IL-1β, 5ng/mL,8h, Bleomycin, 5μg/mL, 8h) induction, cells were treated with either D+Q (Dasatinib, 200nM plus Quercetin, 10 μm) or MβCD@ICAM1-NPs for 24 hours (MβCD 50μg/mL), followed by parallel qPCR analysis of related genes and ELISA quantification of secreted proteins. c, ELISA results of inflammatory mediators (IL-6, Mmp9, Mmp13, Ccl2) and DAMPs (Hmgb1) in conditioned media from senolytic- or NP-treated senescence (IL-1β) group. n=8 biologically independent cell cultures (mean ± s.d.). d, Workflow for detecting the effects of the two therapies on normal proliferating primary chondrocytes for 4 days: qPCR analysis of collected cells and

ELISA quantification of secreted proteins in supernatants. e, Trends of secretion levels of IL-6, Mmp9, Mmp13 and Ccl2 in the supernatant across two therapies (n=4, mean ± s.d.). f, Trends of qPCR results of *IL-6*, *Mmp13*, *Col2a1* and *Aggrecan* in cells across two treatments (n=3, mean ± s.d.). g, Flow chart of the friction coefficient detection under different treatments. Fresh control or OA implants from the same part was collected, and the overall friction coefficient was detected after incubated with senolytics (D+Q) or MINH for 24 hours. h, COF-time curves (1200s) across treatment groups. i, Schematic diagram of in vivo therapeutic comparison using p16-3MR mice. j, Quantitative analysis of 50% paw withdraw threshold across groups. n=8 mice per group (mean ± s.d.). k, Visualization results of the medial subchondral bone plate in each group(top) and the 3D reconstruction of murine knee joints (bottom). The heatmap shows its bone density distribution. Yellow arrows indicate osteophyte formation. l, Representative images of Safranin-O staining results of knee joint sections across groups. The same position (black dashed box) in the above figure is enlarged and shown below (scale bar, 50μm). m, Representative images of immunohistochemical staining (Aggrecan, Col2a1, IL-6 and Mmp13) of medial tibia sections of knee joints across groups (scale bar, 50μm). *P* values were determined using one-way ANOVA with a Tukey post-hoc test (c,j). Source data are provided as a Source Data file.

NCOMMS-25-40829C – Qi

EDITORIAL SUMMARY

Ji, He, Cai, and colleagues report an engineered senescence therapy that exploits lipid metabolic features of senescent cells, repurposing excess lipids as functional resources to improve joint function, and thus alleviating osteoarthritis without eliminating the cells.

Peer Review Information: *Nature Communications* thanks Fernando de la Cuesta and Jing Xie for their contribution to the peer review of this work. A peer review file is available.

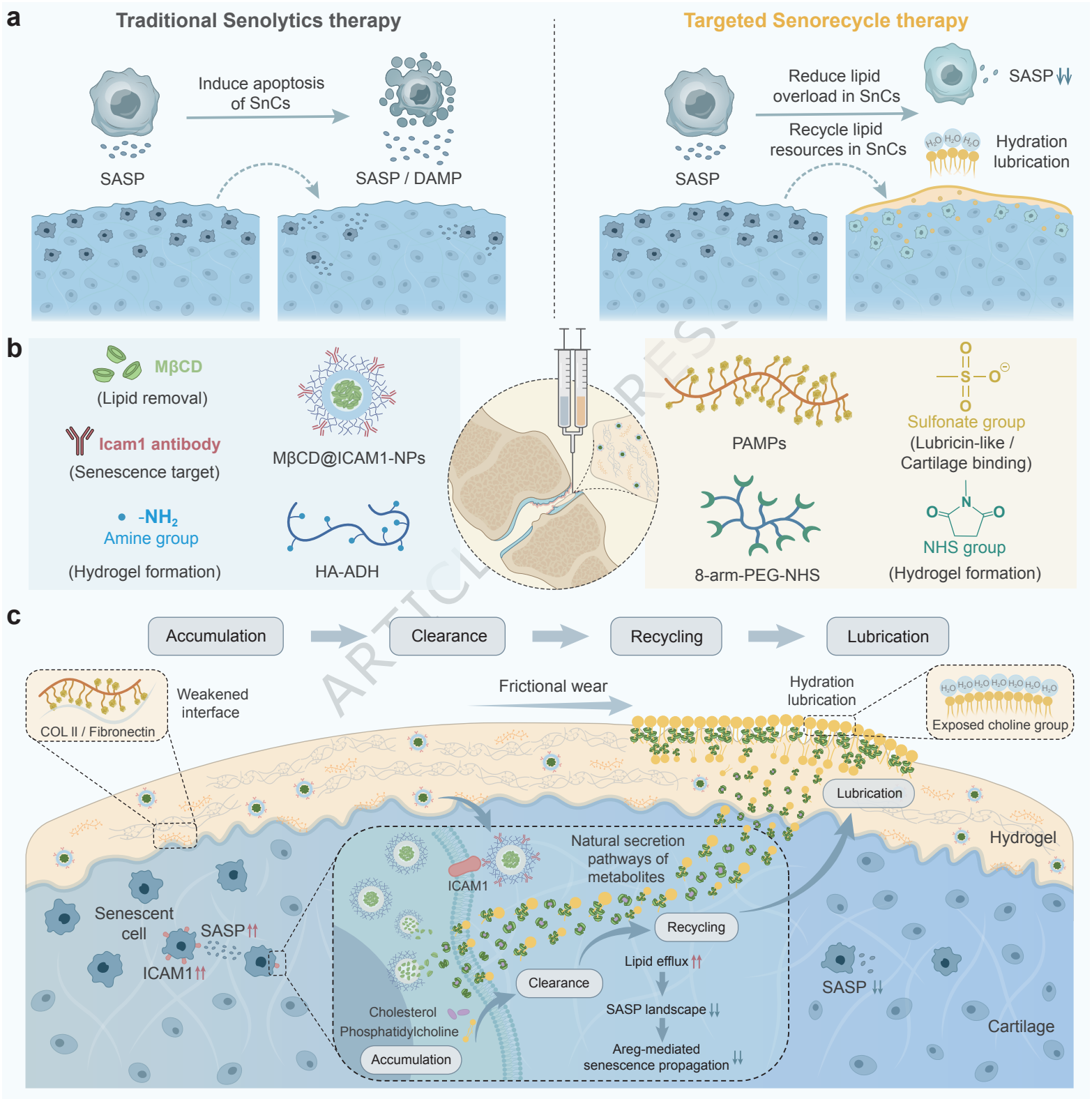
a
Traditional Senolytics therapy
Induce apoptosis of SnCs
SASP
SASP / DAMP
Targeted Senorecycle therapy
Reduce lipid overload in SnCs
Recycle lipid resources in SnCs
SASP
Hydration lubrication
SASP
b
MβCD
(Lipid removal)
Icam1 antibody
(Senescence target)
-NH2
Amine group
(Hydrogel formation)
MβCD@ICAM1-NPs
HA-ADH
PAMPs
8-arm-PEG-NHS
Sulfonate group
(Lubricin-like / Cartilage binding)
NHS group
(Hydrogel formation)
c
Accumulation
Clearance
Recycling
Lubrication
COL II / Fibronectin
Weakened interface
Frictional wear
Hydration lubrication
Exposed choline group
Lubrication
Hydrogel
Natural secretion pathways of metabolites
ICAM1
Senescent cell
SASP
ICAM1
Recycling
Lipid efflux
Clearance
SASP landscape
Areg-mediated senescence propagation
Cholesterol
Phosphatidylcholine
Accumulation
SASP
Cartilage

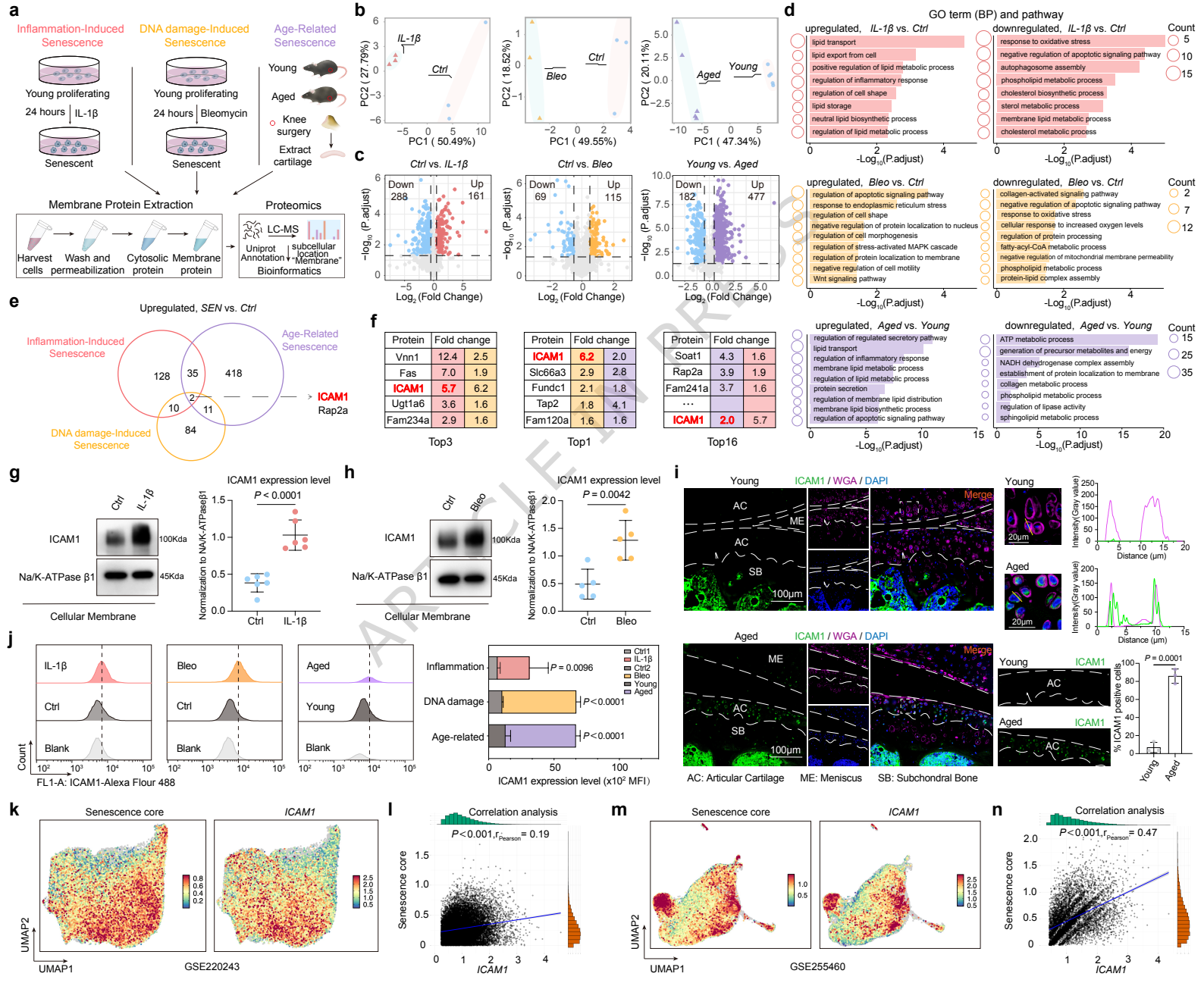
a
Inflammation-Induced Senescence
DNA damage-Induced Senescence
Age-Related Senescence
Young proliferating
24 hours | IL-1β
Senescent
Young proliferating
24 hours | Bleomycin
Senescent
Young
Aged
Knee surgery
Extract cartilage
Membrane Protein Extraction
Harvest cells
Wash and permeabilization
Cytosolic protein
Membrane protein
Proteomics
LC-MS
Uniprot Annotation
subcellular location "Membrane"
Bioinformatics
b
IL-1β
Ctrl
PC1 (50.49%)
PC2 (27.79%)
Bleo
Ctrl
PC1 (49.55%)
PC2 (18.52%)
Aged
Young
PC1 (47.34%)
PC2 (20.11%)
c
Ctrl vs. IL-1β
Down 288
Up 161
Ctrl vs. Bleo
Down 69
Up 115
Young vs. Aged
Down 182
Up 477
-log10 (P.adjust)
Log2 (Fold Change)
d
GO term (BP) and pathway
upregulated, IL-1β vs. Ctrl
lipid transport
lipid export from cell
positive regulation of lipid metabolic process
regulation of inflammatory response
regulation of cell shape
lipid storage
neutral lipid biosynthetic process
regulation of lipid metabolic process
downregulated, IL-1β vs. Ctrl
response to oxidative stress
negative regulation of apoptotic signaling pathway
autophagosome assembly
phospholipid metabolic process
cholesterol biosynthetic process
sterol metabolic process
membrane lipid metabolic process
cholesterol metabolic process
Count
-Log10(P.adjust)
upregulated, Bleo vs. Ctrl
regulation of apoptotic signaling pathway
response to endoplasmic reticulum stress
regulation of cell shape
negative regulation of protein localization to nucleus
regulation of cell morphogenesis
regulation of stress-activated MAPK cascade
regulation of protein localization to membrane
negative regulation of cell motility
Wnt signaling pathway
downregulated, Bleo vs. Ctrl
collagen-activated signaling pathway
negative regulation of apoptotic signaling pathway
response to oxidative stress
cellular response to increased oxygen levels
regulation of protein processing
fatty-acyl-CoA metabolic process
negative regulation of mitochondrial membrane permeability
phospholipid metabolic process
protein-lipid complex assembly
upregulated, Aged vs. Young
regulation of regulated secretory pathway
lipid transport
regulation of inflammatory response
membrane lipid metabolic process
regulation of lipid metabolic process
protein secretion
regulation of membrane lipid distribution
membrane lipid biosynthetic process
regulation of apoptotic signaling pathway
downregulated, Aged vs. Young
ATP metabolic process
generation of precursor metabolites and energy
NADH dehydrogenase complex assembly
establishment of protein localization to membrane
collagen metabolic process
phospholipid metabolic process
regulation of lipase activity
sphingolipid metabolic process
e
Upregulated, SEN vs. Ctrl
Inflammation-Induced Senescence
Age-Related Senescence
DNA damage-Induced Senescence
128
35
418
2
10
11
84
ICAM1
Rap2a
f
Top3
Protein | Fold change
Vnn1 | 12.4 | 2.5
Fas | 7.0 | 1.9
ICAM1 | 5.7 | 6.2
Ugt1a6 | 3.6 | 1.6
Fam234a | 2.9 | 1.6
Top1
Protein | Fold change
ICAM1 | 6.2 | 2.0
Slc66a3 | 2.9 | 2.8
Fundc1 | 2.1 | 1.8
Tap2 | 1.8 | 4.1
Fam120a | 1.6 | 1.6
Top16
Protein | Fold change
Soat1 | 4.3 | 1.6
Rap2a | 3.9 | 1.9
Fam241a | 3.7 | 1.6
…
ICAM1 | 2.0 | 5.7
g
Ctrl
IL-1β
ICAM1
Na/K-ATPase β1
100Kda
45Kda
Cellular Membrane
ICAM1 expression level
P < 0.0001
Normalization to NA/K-ATPaseβ1
h
Ctrl
Bleo
ICAM1
Na/K-ATPase β1
100Kda
45Kda
Cellular Membrane
ICAM1 expression level
P = 0.0042
Normalization to NA/K-ATPaseβ1
i
Young
ICAM1 / WGA / DAPI
AC
ME
SB
100μm
Merge
20μm
Intensity(Gray value)
Distance (μm)
Aged
ICAM1 / WGA / DAPI
AC: Articular Cartilage
ME: Meniscus
SB: Subchondral Bone
P = 0.0001
% ICAM1 positive cells
j
IL-1β
Ctrl
Blank
Bleo
Aged
Young
Count
FL1-A: ICAM1-Alexa Flour 488
Inflammation
DNA damage
Age-related
P = 0.0096
P<0.0001
P<0.0001
Ctrl1
IL-1β
Ctrl2
Bleo
Young
Aged
ICAM1 expression level (x10² MFI)
k
Senescence core
ICAM1
UMAP2
UMAP1
GSE220243
l
Correlation analysis
P<0.001,r Pearson = 0.19
Senescence core
ICAM1
m
Senescence core
ICAM1
UMAP2
UMAP1
GSE255460
n
Correlation analysis
P<0.001,r Pearson = 0.47
Senescence core
ICAM1

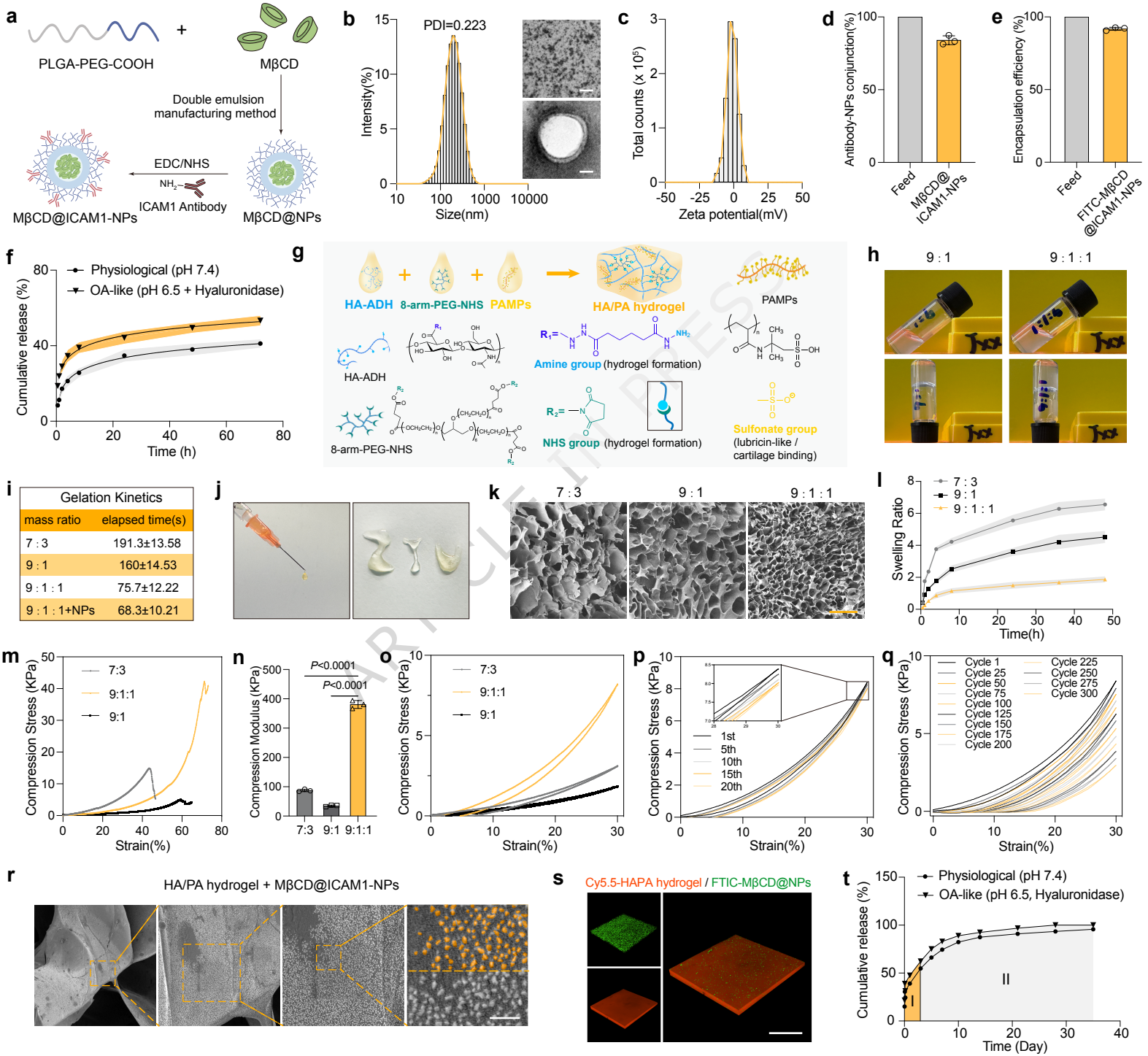
a
PLGA-PEG-COOH
+
MβCD
Double emulsion manufacturing method
EDC/NHS
NH2
ICAM1 Antibody
MβCD@ICAM1-NPs
MβCD@NPs
b
PDI=0.223
Intensity(%)
Size(nm)
c
Total counts (x 10^5)
Zeta potential(mV)
d
Antibody-NPs conjunction(%)
Feed
MβCD@ICAM1-NPs
e
Encapsulation efficiency (%)
Feed
FITC-MβCD@ICAM1-NPs
f
Physiological (pH 7.4)
OA-like (pH 6.5 + Hyaluronidase)
Cumulative release (%)
Time (h)
g
HA-ADH
8-arm-PEG-NHS
PAMPs
HA/PA hydrogel
Amine group (hydrogel formation)
NHS group (hydrogel formation)
Sulfonate group (lubricin-like / cartilage binding)
h
9 : 1
9 : 1 : 1
i
Gelation Kinetics
mass ratio | elapsed time(s)
7 : 3 | 191.3±13.58
9 : 1 | 160±14.53
9 : 1 : 1 | 75.7±12.22
9 : 1 : 1+NPs | 68.3±10.21
j
k
7 : 3
9 : 1
9 : 1 : 1
l
7 : 3
9 : 1
9 : 1 : 1
Swelling Ratio
Time(h)
m
7:3
9:1:1
9:1
Compression Stress (KPa)
Strain(%)
n
P<0.0001
P<0.0001
Compression Modulus (KPa)
7:3
9:1
9:1:1
o
7:3
9:1:1
9:1
Compression Stress (KPa)
Strain(%)
p
1st
5th
10th
15th
20th
Compression Stress (KPa)
Strain(%)
q
Cycle 1
Cycle 25
Cycle 50
Cycle 75
Cycle 100
Cycle 125
Cycle 150
Cycle 175
Cycle 200
Cycle 225
Cycle 250
Cycle 275
Cycle 300
Compression Stress (KPa)
Strain(%)
r
HA/PA hydrogel + MβCD@ICAM1-NPs
s
Cy5.5-HAPA hydrogel / FTIC-MβCD@NPs
t
Physiological (pH 7.4)
OA-like (pH 6.5, Hyaluronidase)
Cumulative release (%)
I
II
Time (Day)

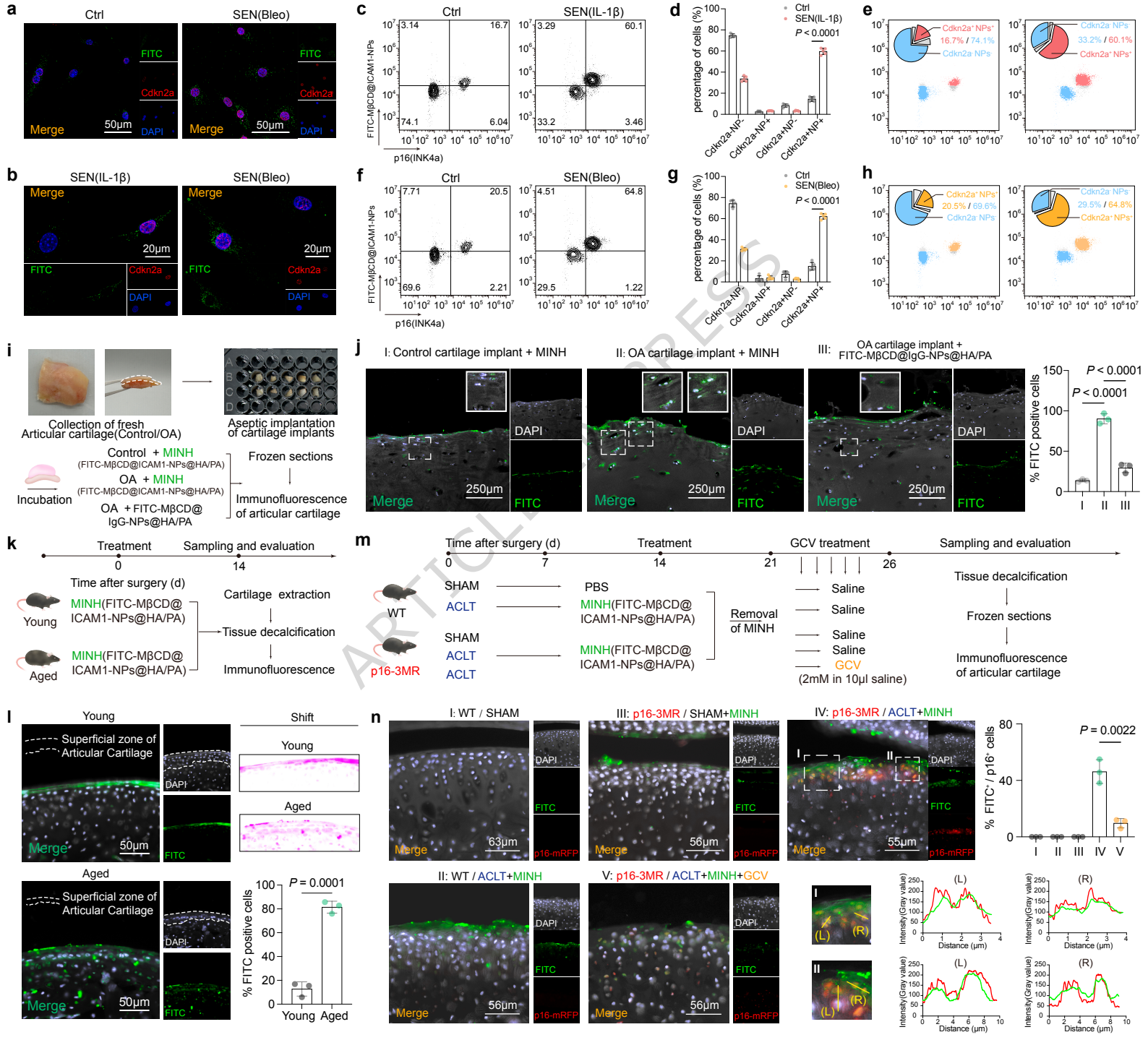
a
Ctrl
SEN(Bleo)
FITC
Cdkn2a
DAPI
Merge
50μm
b
SEN(IL-1β)
SEN(Bleo)
20μm
c
Ctrl
SEN(IL-1β)
FITC-MβCD@ICAM1-NPs
p16(INK4a)
3.14
16.7
74.1
6.04
3.29
60.1
33.2
3.46
d
percentage of cells (%)
Ctrl
SEN(IL-1β)
P < 0.0001
Cdkn2a-NP-
Cdkn2a-NP+
Cdkn2a+NP-
Cdkn2a+NP+
e
Cdkn2a+ NPs+
16.7% / 74.1%
Cdkn2a- NPs-
Cdkn2a- NPs+
33.2% / 60.1%
Cdkn2a+ NPs+
f
Ctrl
SEN(Bleo)
7.71
20.5
69.6
2.21
4.51
64.8
29.5
1.22
g
SEN(Bleo)
h
20.5% / 69.6%
29.5% / 64.8%
i
Collection of fresh
Articular cartilage(Control/OA)
Aseptic implantation
of cartilage implants
Incubation
Control + MINH
(FITC-MβCD@ICAM1-NPs@HA/PA)
OA + MINH
(FITC-MβCD@ICAM1-NPs@HA/PA)
OA + FITC-MβCD@
IgG-NPs@HA/PA
Frozen sections
Immunofluorescence
of articular cartilage
j
I: Control cartilage implant + MINH
II: OA cartilage implant + MINH
III: OA cartilage implant +
FITC-MβCD@IgG-NPs@HA/PA
DAPI
Merge
FITC
250μm
P < 0.0001
P < 0.0001
% FITC positive cells
k
Treatment
Sampling and evaluation
0
14
Time after surgery (d)
Young
Aged
MINH(FITC-MβCD@
ICAM1-NPs@HA/PA)
Cartilage extraction
Tissue decalcification
Immunofluorescence
m
Time after surgery (d)
Treatment
GCV treatment
Sampling and evaluation
0
7
14
21
26
WT
p16-3MR
SHAM
ACLT
PBS
MINH(FITC-MβCD@
ICAM1-NPs@HA/PA)
Removal
of MINH
Saline
GCV
(2mM in 10μl saline)
Tissue decalcification
Frozen sections
Immunofluorescence
of articular cartilage
l
Young
Aged
Superficial zone of
Articular Cartilage
DAPI
FITC
Merge
50μm
Shift
P = 0.0001
% FITC positive cells
Young
Aged
n
I: WT / SHAM
III: p16-3MR / SHAM+MINH
IV: p16-3MR / ACLT+MINH
II: WT / ACLT+MINH
V: p16-3MR / ACLT+MINH+GCV
p16-mRFP
63μm
56μm
55μm
P = 0.0022
% FITC- / p16- cells
(L)
(R)
Intensity(Gray value)
Distance (μm)

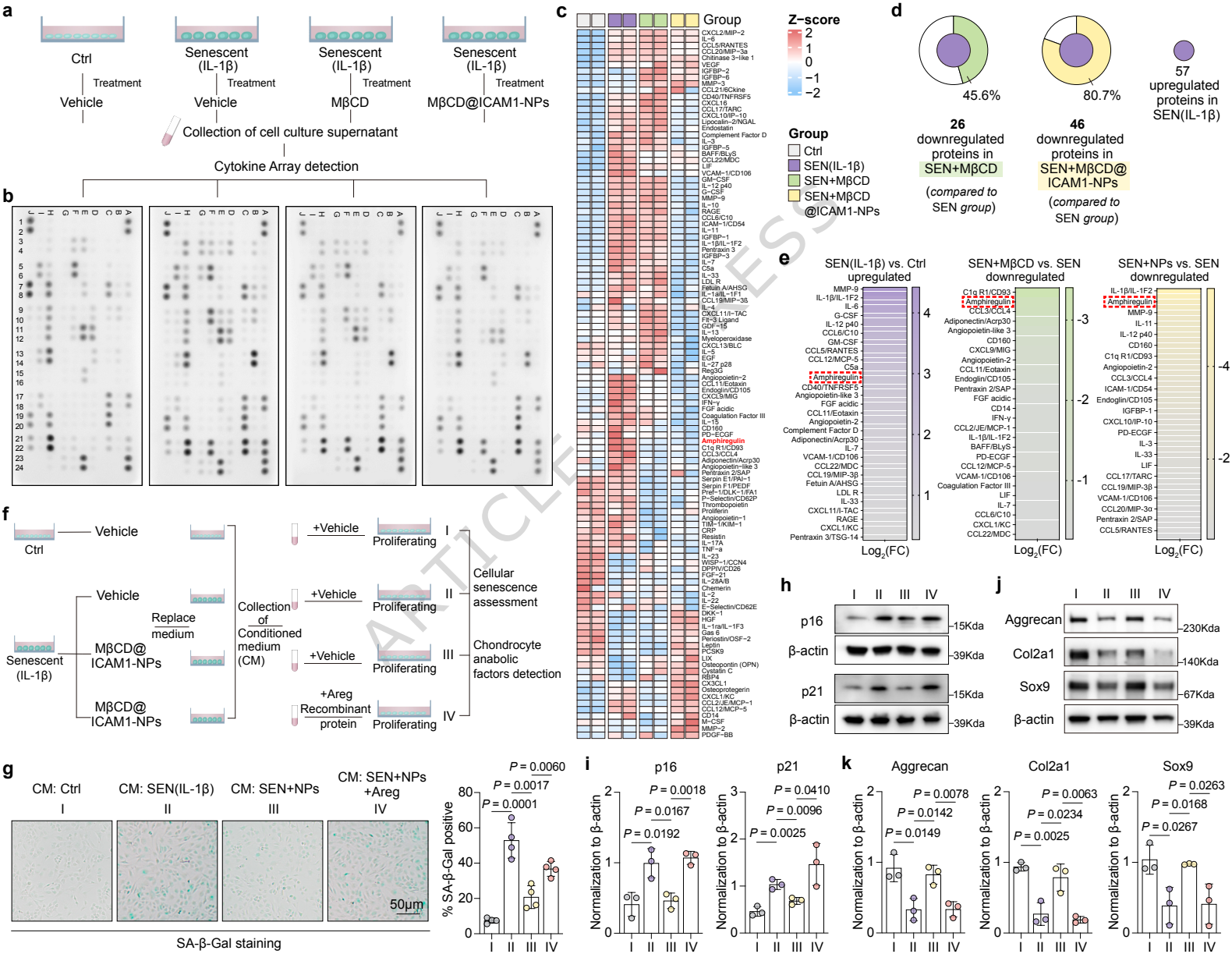
a
Ctrl
Treatment
Vehicle
Senescent (IL-1β)
Treatment
Vehicle
Senescent (IL-1β)
Treatment
MβCD
Senescent (IL-1β)
Treatment
MβCD@ICAM1-NPs
Collection of cell culture supernatant
Cytokine Array detection
b
c
Group
Z-score
2
1
0
−1
−2
Group
Ctrl
SEN(IL-1β)
SEN+MβCD
SEN+MβCD @ICAM1-NPs
d
45.6%
26 downregulated proteins in SEN+MβCD (compared to SEN group)
80.7%
46 downregulated proteins in SEN+MβCD@ ICAM1-NPs (compared to SEN group)
57 upregulated proteins in SEN(IL-1β)
e
SEN(IL-1β) vs. Ctrl upregulated
SEN+MβCD vs. SEN downregulated
SEN+NPs vs. SEN downregulated
Log2(FC)
f
Ctrl
Vehicle
Senescent (IL-1β)
Vehicle
Replace medium
MβCD@ ICAM1-NPs
MβCD@ ICAM1-NPs
Collection of Conditioned medium (CM)
+Vehicle
Proliferating
I
+Vehicle
Proliferating
II
+Vehicle
Proliferating
III
+Areg Recombinant protein
Proliferating
IV
Cellular senescence assessment
Chondrocyte anabolic factors detection
g
CM: Ctrl
I
CM: SEN(IL-1β)
II
CM: SEN+NPs
III
CM: SEN+NPs +Areg
IV
50μm
SA-β-Gal staining
% SA-β-Gal positive
P = 0.0060
P = 0.0017
P = 0.0001
h
p16
β-actin
p21
β-actin
15Kda
39Kda
15Kda
39Kda
i
p16
p21
Normalization to β-actin
P = 0.0018
P = 0.0167
P = 0.0192
P = 0.0410
P = 0.0096
P = 0.0025
j
Aggrecan
Col2a1
Sox9
β-actin
230Kda
140Kda
67Kda
39Kda
k
Aggrecan
Col2a1
Sox9
Normalization to β-actin
P = 0.0078
P = 0.0142
P = 0.0149
P = 0.0063
P = 0.0234
P = 0.0025
P = 0.0263
P = 0.0168
P = 0.0267

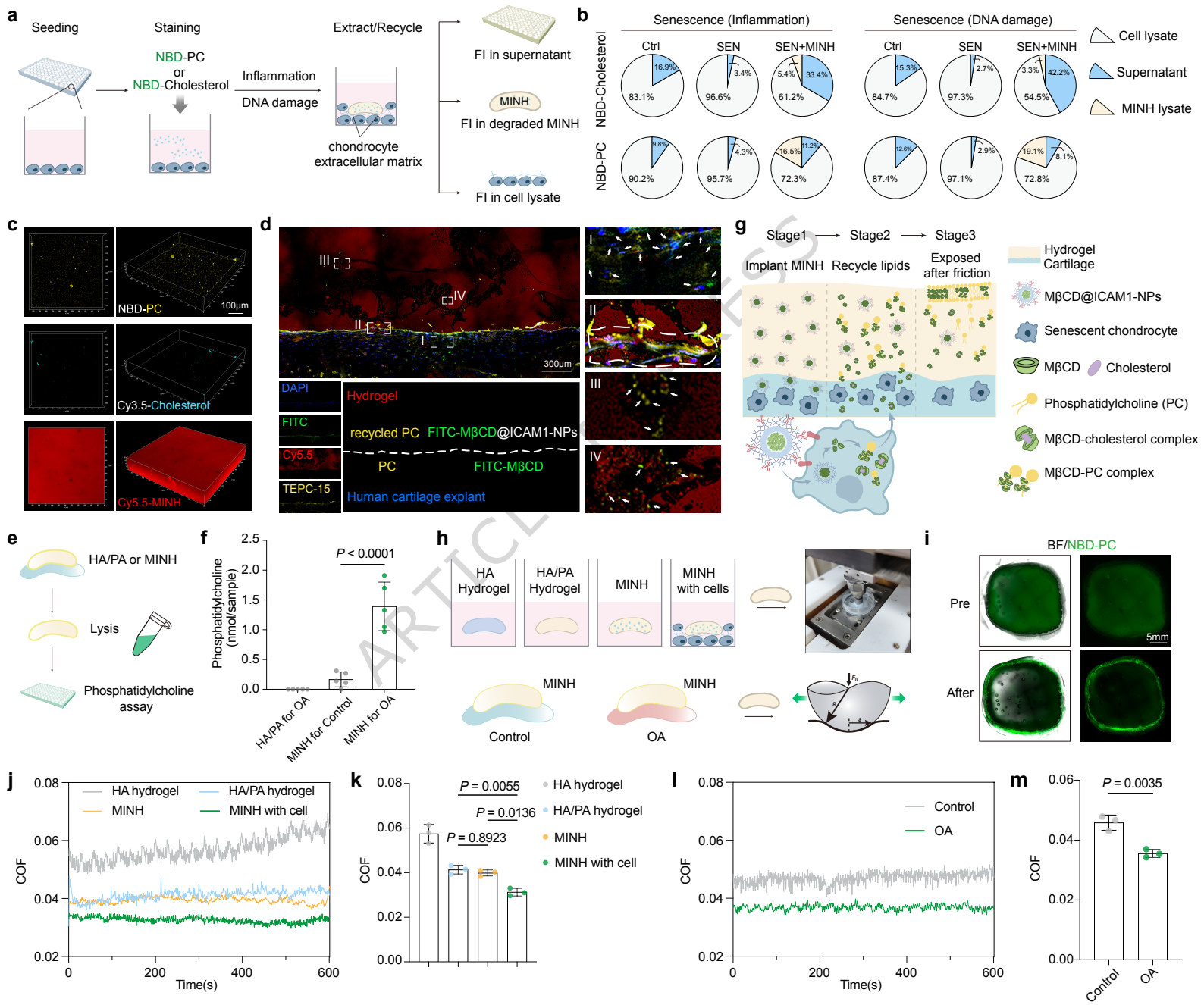
a
Seeding
Staining
NBD-PC
or
NBD-Cholesterol
Inflammation
DNA damage
Extract/Recycle
chondrocyte
extracellular matrix
FI in supernatant
MINH
FI in degraded MINH
FI in cell lysate
b
Senescence (Inflammation)
Senescence (DNA damage)
Ctrl
SEN
SEN+MINH
NBD-Cholesterol
NBD-PC
16.9%
83.1%
3.4%
96.6%
5.4%
33.4%
61.2%
15.3%
84.7%
2.7%
97.3%
3.3%
42.2%
54.5%
9.8%
90.2%
4.3%
95.7%
16.5%
11.2%
72.3%
12.6%
87.4%
2.9%
97.1%
19.1%
8.1%
72.8%
Cell lysate
Supernatant
MINH lysate
c
NBD-PC
100μm
Cy3.5-Cholesterol
Cy5.5-MINH
d
III
IV
II
I
300μm
DAPI
FITC
Cy5.5
TEPC-15
Hydrogel
recycled PC
FITC-MβCD@ICAM1-NPs
PC
FITC-MβCD
Human cartilage explant
g
Stage1
Stage2
Stage3
Implant MINH
Recycle lipids
Exposed
after friction
Hydrogel
Cartilage
MβCD@ICAM1-NPs
Senescent chondrocyte
MβCD
Cholesterol
Phosphatidylcholine (PC)
MβCD-cholesterol complex
MβCD-PC complex
e
HA/PA or MINH
Lysis
Phosphatidylcholine
assay
f
P < 0.0001
Phosphatidylcholine
(nmol/sample)
2.5
2.0
1.5
1.0
0.5
0.0
HA/PA for OA
MINH for Control
MINH for OA
h
HA
Hydrogel
HA/PA
Hydrogel
MINH
MINH
with cells
MINH
Control
MINH
OA
i
BF/NBD-PC
Pre
After
5mm
j
HA hydrogel
HA/PA hydrogel
MINH
MINH with cell
COF
0.08
0.06
0.04
0.02
0
200
400
600
Time(s)
k
P = 0.0055
P = 0.0136
P = 0.8923
HA hydrogel
HA/PA hydrogel
MINH
MINH with cell
COF
0.08
0.06
0.04
0.02
0.00
l
Control
OA
COF
0.08
0.06
0.04
0.02
0
200
400
600
Time(s)
m
P = 0.0035
COF
0.06
0.04
0.02
0.00
Control
OA

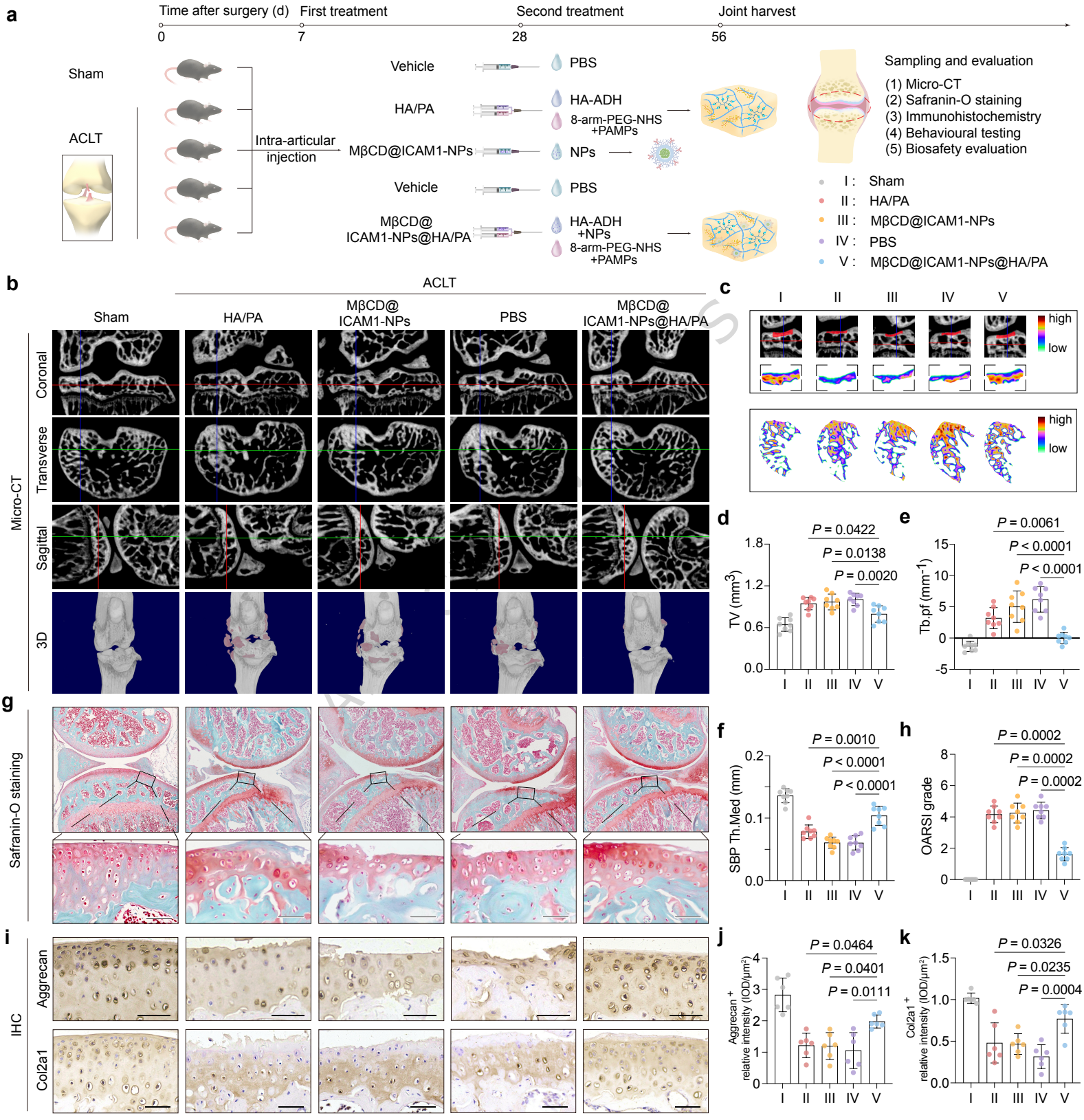
a
Time after surgery (d)
First treatment
Second treatment
Joint harvest
0
7
28
56
Sham
ACLT
Intra-articular injection
Vehicle
PBS
HA/PA
HA-ADH
8-arm-PEG-NHS +PAMPs
MβCD@ICAM1-NPs
NPs
Vehicle
PBS
MβCD@ ICAM1-NPs@HA/PA
HA-ADH +NPs
8-arm-PEG-NHS +PAMPs
Sampling and evaluation
(1) Micro-CT
(2) Safranin-O staining
(3) Immunohistochemistry
(4) Behavioural testing
(5) Biosafety evaluation
I : Sham
II : HA/PA
III : MβCD@ICAM1-NPs
IV : PBS
V : MβCD@ICAM1-NPs@HA/PA
b
ACLT
Sham
HA/PA
MβCD@ ICAM1-NPs
PBS
MβCD@ ICAM1-NPs@HA/PA
Micro-CT
Coronal
Transverse
Sagittal
3D
c
I
II
III
IV
V
high
low
d
P = 0.0422
P = 0.0138
P = 0.0020
TV (mm3)
e
P = 0.0061
P < 0.0001
P < 0.0001
Tb.pf (mm-1)
g
Safranin-O staining
f
P = 0.0010
P < 0.0001
P < 0.0001
SBP Th.Med (mm)
h
P = 0.0002
P = 0.0002
P = 0.0002
OARSI grade
i
IHC
Aggrecan
Col2a1
j
P = 0.0464
P = 0.0401
P = 0.0111
Aggrecan+ relative intensity (IOD/μm2)
k
P = 0.0326
P = 0.0235
P = 0.0004
Col2a1+ relative intensity (IOD/μm2)

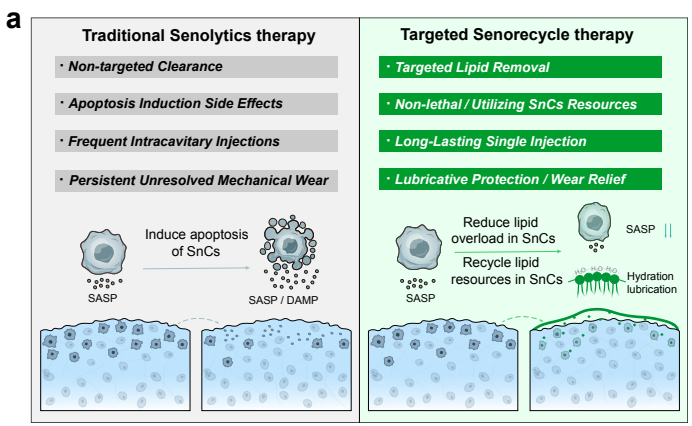
a
Traditional Senolytics therapy
· Non-targeted Clearance
· Apoptosis Induction Side Effects
· Frequent Intracavitary Injections
· Persistent Unresolved Mechanical Wear
Induce apoptosis of SnCs
SASP
SASP / DAMP
Targeted Senorecycle therapy
· Targeted Lipid Removal
· Non-lethal / Utilizing SnCs Resources
· Long-Lasting Single Injection
· Lubricative Protection / Wear Relief
Reduce lipid overload in SnCs
Recycle lipid resources in SnCs
SASP
SASP
Hydration lubrication

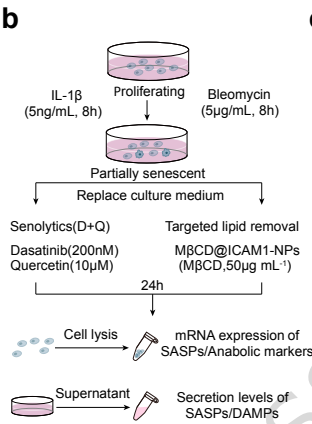
b
Proliferating
IL-1β (5ng/mL, 8h)
Bleomycin (5μg/mL, 8h)
Partially senescent
Replace culture medium
Senolytics(D+Q)
Dasatinib(200nM) Quercetin(10μM)
Targeted lipid removal
MβCD@ICAM1-NPs (MβCD,50μg mL⁻¹)
24h
Cell lysis
mRNA expression of SASPs/Anabolic markers
Supernatant
Secretion levels of SASPs/DAMPs

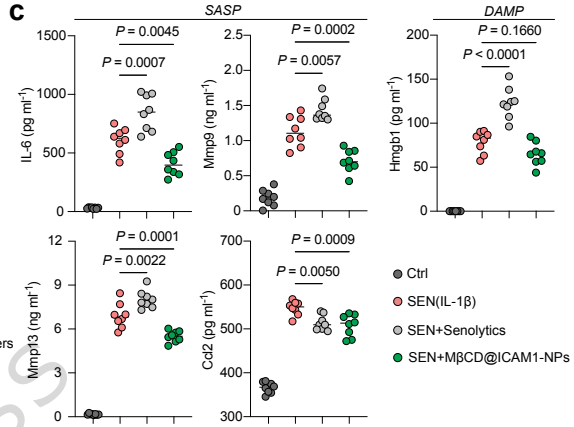
c
SASP
DAMP
IL-6 (pg ml⁻¹)
Mmp9 (ng ml⁻¹)
Hmgb1 (pg ml⁻¹)
Mmp13 (ng ml⁻¹)
Ccl2 (pg ml⁻¹)
P = 0.0045
P = 0.0007
P = 0.0002
P = 0.0057
P = 0.1660
P < 0.0001
P = 0.0001
P = 0.0022
P = 0.0009
P = 0.0050
Ctrl
SEN(IL-1β)
SEN+Senolytics
SEN+MβCD@ICAM1-NPs

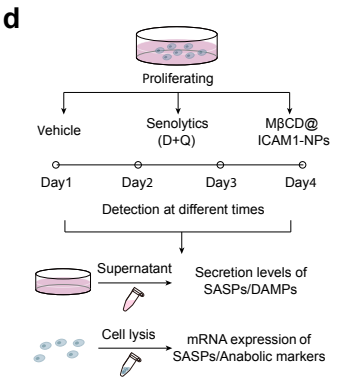
d
Proliferating
Vehicle
Senolytics (D+Q)
MβCD@ICAM1-NPs
Day1
Day2
Day3
Day4
Detection at different times
Supernatant
Secretion levels of SASPs/DAMPs
Cell lysis
mRNA expression of SASPs/Anabolic markers

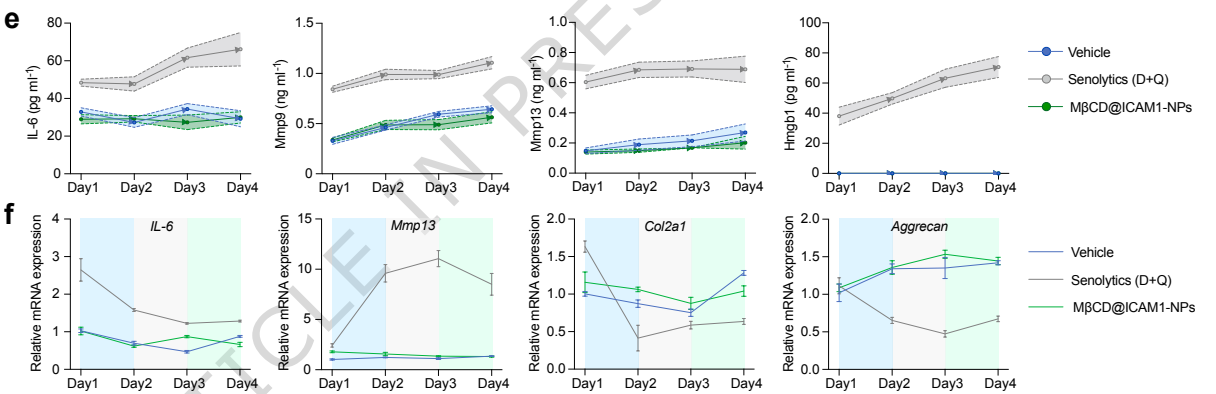
e
IL-6 (pg ml⁻¹)
Mmp9 (ng ml⁻¹)
Mmp13 (ng ml⁻¹)
Hmgb1 (pg ml⁻¹)
Vehicle
Senolytics (D+Q)
MβCD@ICAM1-NPs
f
IL-6
Mmp13
Col2a1
Aggrecan
Relative mRNA expression

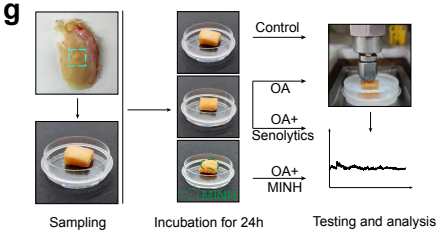
g
Control
OA
OA+ Senolytics
OA+ MINH
Sampling
Incubation for 24h
Testing and analysis

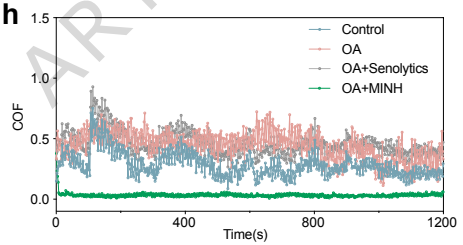
h
COF
Time(s)
Control
OA
OA+Senolytics
OA+MINH

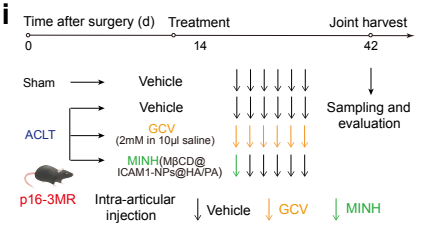
i
Time after surgery (d)
Treatment
Joint harvest
Sham
ACLT
Vehicle
GCV (2mM in 10μl saline)
MINH(MβCD@ICAM1-NPs@HA/PA)
Sampling and evaluation
p16-3MR
Intra-articular injection
Vehicle
GCV
MINH

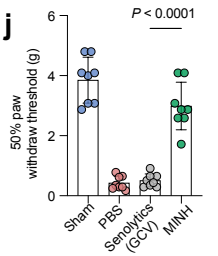
j
P < 0.0001
50% paw withdraw threshold (g)
Sham
PBS
Senolytics (GCV)
MINH

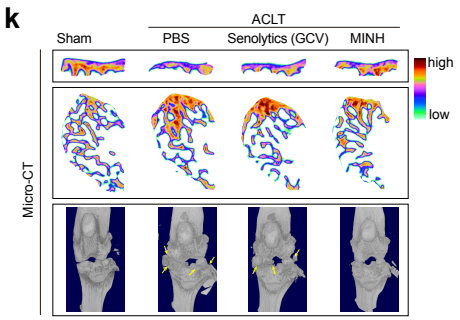
k
Sham
ACLT
PBS
Senolytics (GCV)
MINH
high
low
Micro-CT

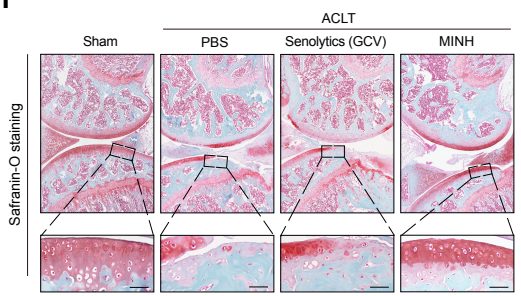
l
Sham
ACLT
PBS
Senolytics (GCV)
MINH
Safranin-O staining

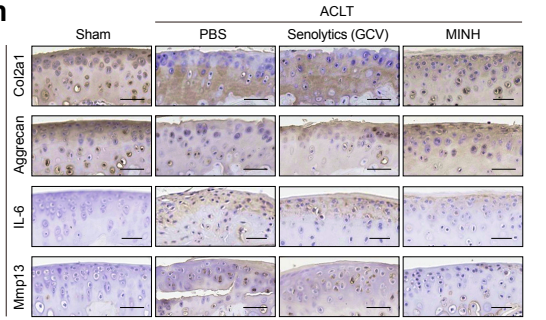
m
Sham
ACLT
PBS
Senolytics (GCV)
MINH
Col2a1
Aggrecan
IL-6
Mmp13
IHC